Cholesterol regulates plasma membrane bending by prominin-family proteins

Tristan A. Bell[1,2]*, Bridget E. Luce[1], Pusparanee Hakim[1], Hiba Dardari[1], Virly Y. Ananda[1], Tran H. Nguyen[1], Arezu Monshizadeh[1], and Luke H. Chao[1,2]*

[1]Department of Molecular Biology, Massachusetts General Hospital, Boston, MA, 02114

[2]Department of Genetics, Blavatnik Institute, Harvard Medical School, Boston, MA, 02115

*For correspondence: Tristan Bell, 185 Cambridge St., CPZN 7250, Boston, MA, 02114, bell@molbio.mgh.harvard.edu, (916) 740-5218; Luke Chao, 185 Cambridge St., CPZN 7250, Boston, MA, 02114, chao@molbio.mgh.harvard.edu, (617) 724-3324

Running Title: Cholesterol-dependent regulation of Prominin

Major Classification: Biological Sciences

Minor Classification: Biochemistry

Keywords: prominin-1, extracellular vesicles, membrane biophysics, protein conformation, cholesterol-binding protein

Preprint Servers: Deposited with bioRxiv under a CC-BY 4.0 license (BIORXIV/2023/566258)

Abstract

Prominin-1 (Prom1) is a pentaspan membrane protein that associates with curved regions of the plasma membrane. Prom1 localizes to cholesterol-rich domains and requires membrane cholesterol to support membrane remodeling. Membrane bending activity is particularly evident in photoreceptors, where Prom1 mutations cause loss of outer segment disk homeostasis leading to cone-rod retinal dystrophy (CCRD). However, the mechanistic link between prominin-dependent cholesterol binding, membrane remodeling, and retinal disease remains unclear. Here, we characterize the membrane bending function and specific cholesterol binding activity of Prom1 and its proposed homolog Tweety homology 1 (Ttyh1) in extracellular vesicles (EVs). Prom1 and Ttyh1 induce formation of EVs in cultured mammalian cells that are biophysically similar. Though both proteins bend membranes and form EVs at the plasma membrane, Ttyh1 lacks a stable interaction with cholesterol that is present in Prom1. Correspondingly, Ttyh1 forms EVs that are more deformed than those produced by Prom1. An evolutionarily conserved and retinal disease-associated Prom1 residue (Trp-795) is necessary for cholesterol binding, EV membrane

deformation, and efficient trafficking to the plasma membrane. Removal of *N*-glycan moieties from Prom1 biases the enzyme toward a cholesterol-bound state. We propose that Prom1 and Ttyh1 are both members of a single prominin family of membrane bending proteins, that Ttyh1 is a constitutively active member of this family, and that Prom1 is regulated by cholesterol binding and *N*-glycosylation. These findings shed light on mechanisms of prominin family function in disease and help unify models of prominin function across diverse cell types.

Significance Statement

Mammalian cells dynamically shape the plasma membrane to achieve specialized functions. Prominin-1 (Prom1) is a membrane protein that promotes bending and shaping of the membrane, notably in photoreceptors. Here, the authors find that membrane cholesterol regulates the membrane bending activity of Prom1 in extracellular vesicles. Membrane bending can be tuned by altering cholesterol levels and may be coupled to different Prom1 *N*-glycosylation states. A distant homolog of Prom1 called Ttyh1 is also shown to form extracellular vesicles and supports more membrane bending than Prom1 though it does not bind cholesterol. This work unites the Prom and Ttyh protein families into a single functional group and helps explain how membrane cholesterol functionalizes prominin-family proteins for different roles in different cell types.

Introduction

Mammalian cells interact with the extracellular environment through proteins, lipids, and glycans at the plasma membrane. Organized protrusive structures of the membrane such as microvilli and cilia are hotspots for nutrient absorption, cell cycle regulation, and extracellular signaling[1,2]. Membrane protrusions are organized both by interactions with the cytoskeleton and by sorting of proteins and lipids into membrane microdomains[2–4]. Prominin-1 (Prom1) is a five-transmembrane pass integral membrane protein that localizes specifically to cholesterol-rich membrane microdomains associated with membrane protrusion[5]. Prom1 was first characterized as the target of AC133-1, a monoclonal antibody raised against pluripotent human epithelial stem cells[6,7]. Since then, Prom1 has been identified in the apical membranes of most epithelial and neuroepithelial cell types, but is only natively recognized by AC133-1 in stem cells and photoreceptors[8–10]. In photoreceptors, Prom1 forms complexes with Protocadherin-21 (Pcdh21) that are necessary for normal membrane disc biogenesis[11–19], and several Prom1 mutations associate with hereditary cone-rod retinal dystrophy (CRRD)[11,20–23]. Animals also express at least one paralogous prominin protein (Prominin-2) that is present in most non-retinal cell types[24].

When overexpressed, Prom1 dramatically reorganizes the plasma membrane of cultured mammalian cells into long protrusions[25,26]. Small-molecule inhibitors of actin and tubulin do not impair the tubulation phenotype, indicating that cytoskeletal interactions are not required for membrane bending[25,26]. Accordingly, Prom1 interacts with cholesterol in cell membranes, and cells treated with cholesterol biosynthesis inhibitors or depletion agents do not exhibit membrane tubulation, suggesting that cholesterol regulates Prom1 function[25,26].

Prom1 also induces formation of extracellular vesicles (EVs) that bleb from the apical plasma membrane of differentiating epithelial stem cells[27]. Large Prom1 EVs (500-700 nm in diameter) appear to form from bulk release of membrane from the cell midbody, whereas small Prom1 EVs (< 250 nm in diameter) likely emanate from organized membrane protrusions such as microvilli and cilia[27–29]. Prom1 EVs can be readily detected in saliva, urine, semen, neural tube fluid, and lacrimal fluid of healthy adults[28,30].

Recently, the Tweety homology (Ttyh) protein family was hypothesized to be a distant homolog of the prominins[25]. Ttyh proteins share prominins' five-transmembrane topology but have smaller extracellular domains[31]. Most animals have three paralogous Ttyh proteins (Ttyh1, Ttyh2, and Ttyh3)[32] that all are predominantly expressed in neural tissues[33–38]. Notably, overexpression of Ttyh1 in cultured cells induces plasma membrane tubulation that is strikingly similar to that observed with Prom1[32,39–41].

Understanding Prom1 membrane bending is foundational for understanding retinal disease and stem cell development, but the relationship between Prom1 and cholesterol that underlies membrane reshaping remains unclear. Here, we reconstitute and purify Prom1 EVs to characterize Prom1 function in a native membrane bilayer. Prom1 forms a stable interaction with cholesterol that is resistant to delipidation by nonionic detergent. Mutation of a residue implicated in retinal disease stabilizes cholesterol binding and negatively regulates membrane bending. *N*-glycosylation is also necessary for dynamic cholesterol binding. We further demonstrate that Prom1 homolog Ttyh1 forms EVs similar to Prom1 EVs but does not co-purify with endogenous cholesterol. We propose that cholesterol binding allosterically regulates membrane bending by prominins, and that the Ttyh proteins are prominin family members biased toward constitutive membrane bending activity. These findings contribute to a mechanistic foundation for distinct prominin function in different tissues, including the role of Prom1 in retinal homeostasis and disease.

97

98 **Results**

99 *Reconstitution and purification of Prom1 EVs*

100 To understand how Prom1 interacts with and reshapes native membranes, we sought a method to purify
101 Prom1 without disturbing protein-lipid interactions. Because Prom1 is endogenously detectable in EVs[28],
102 we asked whether Prom1 induces EV formation in a cell culture system. C-terminally strep-tagged Prom1
103 was detected in immunoblots of the conditioned media from transfected cells, but not in cells treated
104 with a no-plasmid mock transfection (Fig 1A, 1B). To validate that the ~120 kDa Strep-reactive band we
105 observe is indeed Prom1-Strep, we immunoblotted with the Prom1-specific antibody AC133-1[42] and
106 observed robust staining (Fig 1C). To confirm that EV production is not an artifact of transfection, we
107 introduced Prom1-Strep into Expi293 cells by lentiviral transduction to generate a stable polyclonal
108 overexpression cell line. A Strep-reactive band consistent with mature Prom1 was detectable in the
109 conditioned media from these cells over several rounds of cell passaging (Fig S1A). We assessed the
110 protein composition of Prom1 EVs using SDS-PAGE and silver nitrate staining. Prom1 was a primary
111 constituent of our samples alongside several other proteins (Fig S1B). We cannot conclude whether these
112 proteins specifically interact with Prom1 in EVs, are hitchhikers enclosed within the EVs, or originate from
113 endogenous co-purifying EVs.

114

115 We next purified the Prom1 EVs using differential centrifugation, ultracentrifugal concentration, and size-
116 exclusion chromatography (SEC) based on isolation methods previously described for endogenous small
117 Prom1 EVs (Fig 1A)[28,43]. Solution size measurement with dynamic light scattering (DLS) indicated that
118 purified Prom1 EVs are monodisperse with an average diameter of 164 ± 14 nm, considerably larger than
119 the 50-80 nm EVs measured by negative-stain transmission electron microscopy (NS-TEM) in samples
120 purified from biological fluids[28] (Fig 1D). Upon treatment with PNGase F, an enzyme that cleaves *N*-glycan
121 groups from proteins, the ~120 kDa Prom1 gel band shifted down to its predicted molecular weight of 102
122 kDa (Fig 1E).

123

124 To verify that the purified particles are truly EVs (secreted particles with intact membrane bilayers), we
125 vitrified purified samples and imaged them using transmission cryo-electron microscopy (cryo-TEM) (Fig
126 1F). We observed spherical EVs with bilayer membranes (Fig 1F, inset). The diameters of EVs measured by
127 cryo-TEM was bimodal with an average diameter of 117 ± 58 nm, somewhat lower than our
128 measurements from DLS (Fig 1H). We next used NS-TEM to directly compare our reconstituted Prom1 EVs

129 with previously characterized endogenous Prom1 EVs[28] (Fig 1G). We observed a distribution of largely
130 circular EVs ranging in size from ~50 nm to ~250 nm in diameter, but more skewed toward smaller
131 diameters than observed in the cryo-TEM data (Fig 1H). In addition, EVs had rough edges and internal
132 depressions in NS-TEM, a characteristic feature of EV fixation[28] (Fig 1H). Because solution DLS
133 measurements (164 ± 14 nm) suggest larger EV diameters than our NS-TEM (123 ± 73 nm) or cryo-TEM
134 (117 ± 58 nm) measurements, we speculate that sample fixation or vitrification may induce deformation
135 and fission in the reconstituted EVs. This effect may have similarly impacted previous characterization of
136 endogenous Prom1 EVs[28]. We conclude that reconstituted Prom1 EVs have similar morphology to
137 endogenous EVs, but may be slightly larger in size.
138
139 We next asked whether Prom1 in purified EVs retains known functional behavior of Prom1 from
140 endogenous membranes. Previous studies established that Prom1 stably binds Pcdh21 in photoreceptor
141 outer segments to stabilize intermembrane tethers[11,12]. To determine if Prom1 can bind Pcdh21 in our EV
142 samples, we co-transfected Expi293 cells with Strep-tagged Prom1 and Flag-tagged Pcdh21 and looked
143 for the presence of each component in cells, conditioned media (CM), and clarified conditioned media
144 (CCM). Pcdh21 was only observed in CCM samples when co-expressed with Prom1, indicating that Prom1
145 is necessary to traffic Pcdh21 into this class of EVs (Fig 1I). To further establish the interaction, we co-
146 expressed Prom1-Strep with mNeonGreen-tagged Pcdh21 and immunopurified Prom1 from EVs
147 solubilized with 1% n-dodecyl-ß-D-maltoside (DDM). Pcdh21-associated mNeonGreen robustly co-
148 purified with detergent-solubilized Prom1 compared to a control condition lacking Prom1, indicating that
149 the two proteins physically interact in purified EVs (Fig 1J).
150

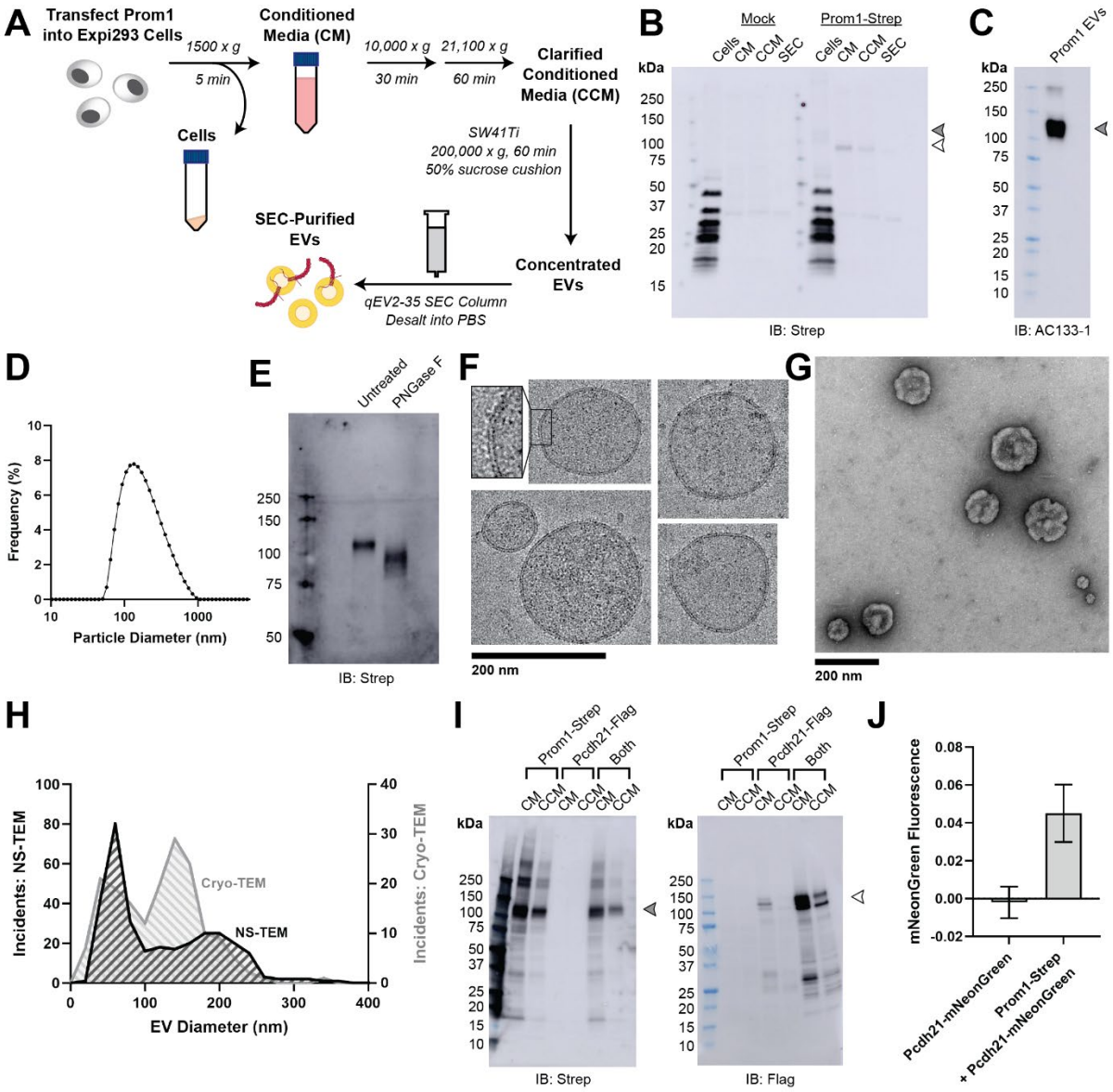

Figure 1. (A) EV expression and purification protocol. **(B)** Anti-Strep immunoblot of cell pellet, conditioned media (CM), clarified conditioned media (CCM), or SEC-purified EVs from mock-transfected or Prom1-Strep-transfected Expi293 cells. Filled and empty arrows indicate expected molecular weights of native and de-glycosylated Prom1, respectively. **(C)** AC133-1 immunoblot of SEC-purified Prom1 EVs. **(D)** Dynamic light scattering measurement of purified Prom1 EV solution size. **(E)** Anti-Strep immunoblot of Prom1 EVs treated with or without PNGase F to remove *N*-glycan moieties. **(F)** Cryo-TEM images of purified Prom1 EVs. Inset image is magnified to emphasize membrane bilayer density. Images are lowpass filtered to 5 Å to enhance contrast. **(G)** NS-TEM images of purified Prom1 EVs. **(H)** Measured diameters of Prom1 EVs from Cryo-TEM or NS-TEM images. (n = 322 and n = 176 for NS-TEM and cryo-TEM measurements, respectively.) **(I)** Anti-Strep (Prom1) and anti-Flag (Pcdh21) immunoblots of CM and CCM from cells transfected with Prom1-Strep, Pcdh21-Flag, or both. Note that Pcdh21 is only detected in CCM when co-expressed with Prom1. Filled and empty arrows indicate expected molecular weights of

164 glycosylated Prom1-Strep and Pcdh21-Flag, respectively. **(J)** Fluorescence measurement of Pcdh21-
165 mNeonGreen co-immunoprecipitated with Prom1-Strep.

166

167 *Mutations in the Prom1 transmembrane domain impair EV formation*

168 Prom1 binds cholesterol in native membranes[26], but it is not known how interaction with cholesterol
169 regulates membrane bending and EV formation. We analyzed the sequence of human Prom1 to identify
170 cholesterol recognition amino acid consensus sequences (CRAC, [L/V]-X_{1-5}-[Y/F]-X_{1-5}-[K/R]) or mirrored
171 CRAC (CARC, [K/R]-X_{1-5}-[Y/F]-X_{1-5}-[L/V]) sequences in the transmembrane domains, as these motifs often
172 predict cholesterol binding in membrane proteins[44]. Human Prom1 contained four CRAC and two CARC
173 motifs, of which none were completely conserved among metazoans and only one (CRAC-3) was modestly
174 evolutionarily conserved (Figs S2A, S2B). We therefore turned to a more comprehensive evolutionary
175 analysis of prominin proteins to identify evolutionarily conserved Prom1 transmembrane residues.

176

177 We curated prominin sequences from across eukaryotes, considering a prominin to be a sequence with
178 five predicted transmembrane helices, two large extracellular loops, two small intracellular loops, and
179 homology to annotated metazoan prominin sequences. Putative prominin sequences were identified
180 across metazoans as well as in fungi, excavates, SAR, and green plants (Figs S3A, S3B). Strikingly, Trp-795
181 was nearly perfectly conserved across metazoa and eukaryotic outgroups, making it by far the most
182 conserved residue (excluding Cys residues positioned to form disulfides in AlphaFold2 models) across the
183 curated prominin sequences (Figs 2A, S6A). This result was of particular interest as a missense mutation
184 at this site (W795R) is implicated in hereditary CCRD cases[45]. We selected Trp-795, Leu-161, Gly-454, and
185 Asn-791 as residues with evolutionary evidence for potential prominin function.

186

187 We generated Prom1-Strep variants with mutations to disrupt each CRAC or CARC motif, point mutations
188 targeting evolutionarily conserved residues, and point mutations directed against residues predicted to
189 be in close contact with Trp-795 in Alphafold2 models (Fig 2B, Table ST1)[46]. We then assessed EV formation
190 by quantifying Prom1-Strep signal secreted in EVs or retained in the cellular membranes. We found that
191 mutations disrupting the CARC-1 or CARC-2 sites decreased the proportion of Prom1 secreted in EVs, as
192 did point mutations to Gly-454 or Trp-795 and neighboring residues (Fig 2C). In most cases, this effect
193 arose from both decreased expression of Prom1 and increased retention of protein in cells. However, the
194 CARC-2 mutant was more highly expressed than WT, with the entire effect arising from cellular membrane
195 retention. To better characterize the morphology of the Prom1 variants, we expressed and purified a

196 subset of mutant Prom1 EVs at larger scale. Each of the mutants produced EVs that DLS analysis indicated
197 to be monodisperse and 150-200 nm in diameter, similar to WT Prom1 EVs (Fig 2D). Thus, transmembrane
198 domain mutations in Prom1 primarily alter the quantity of EVs produced rather than EV size.
199
200 To better understand the mechanism of the reduction in Prom1 EV formation, we engineered HeLa cells
201 stably expressing C-terminally StayGold-tagged WT (Prom1-SG) or W795R Prom1 (Prom1[W795R]-SG)
202 under the EF1a promoter. Prom1-SG signal colocalizes with Wheat Germ Agglutinin (WGA)-stained plasma
203 membrane and intracellular vesicles, but Prom1[W795R]-SG concentrated on WGA-positive intracellular
204 vesicles (Fig 2E). Despite the apparent low signal of plasma-membrane localized Prom1-SG, line scan
205 analysis shows correlation between Prom1-SG signal across the cell junctions (Fig 2F top, Fig S4 left). In
206 contrast, there is a marked absence of Prom1[W795R]-SG signal localized on the plasma membrane (Fig
207 2F bottom, Fig S4 right). We infer that fluorescent WT Prom1 is trafficked to the plasma membrane far
208 more efficiently than the W795R mutant.
209

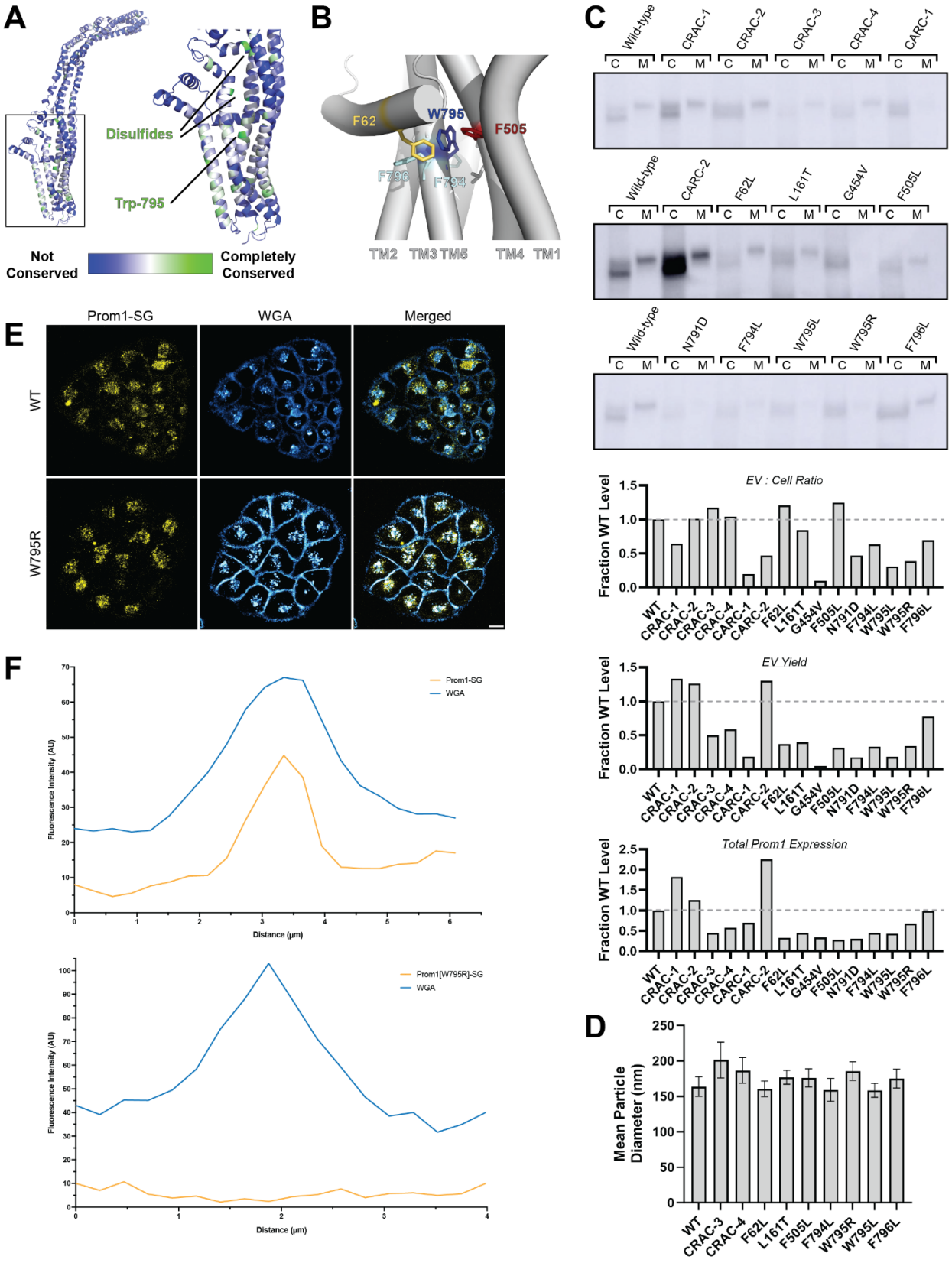
A
Disulfides
Trp-795
Not Conserved
Completely Conserved
B
F62
W795
F505
F796
F794
TM2
TM3
TM5
TM4
TM1
C
Wild-type
CRAC-1
CRAC-2
CRAC-3
CRAC-4
CARC-1
CARC-2
F62L
L161T
G454V
F505L
N791D
F794L
W795L
W795R
F796L
C
M
E
Prom1-SG
WGA
Merged
WT
W795R
F
Prom1-SG
WGA
Fluorescence Intensity (AU)
Distance (µm)
Prom1[W795R]-SG
WGA
Fluorescence Intensity (AU)
Distance (µm)
EV : Cell Ratio
Fraction WT Level
EV Yield
Fraction WT Level
Total Prom1 Expression
Fraction WT Level
D
Mean Particle Diameter (nm)
WT
CRAC-3
CRAC-4
F62L
L161T
F505L
F794L
W795R
W795L
F796L

212 **Figure 2. (A)** AlphaFold2 model of human Prom1[46] with residues color-coded by level of conservation
213 across a representative alignment of metazoan prominin sequences. **(B)** Possible allosteric network
214 between Trp-795 and several adjacent aromatic residues in human Prom1. **(C)** Anti-strep immunoblots
215 of cellular and media (CCM) pools of various Prom1-Strep mutants, and quantification of those signals.
216 **(D)** Mean particle diameter of purified Prom1-Strep EVs measured by dynamic light scattering. Error
217 bars indicate S.D. (n = 5). **(E)** Confocal fluorescence microscopy images of HeLa cells stably expressing
218 WT (top) or W795R (bottom) Prom1-StayGold (yellow), stained with wheat germ agglutinin (WGA)
219 (blue). Scale bar is 10 µm. **(F)** Line scan traces across cell junctions for Prom1-StayGold and WGA signal
220 for WT (top) and W795R (bottom) Prom1.

221

222 *Prom1 mutants adopt different cholesterol binding states*

223 Prom1 localizes to cholesterol-rich microdomains of the plasma membrane.[26] Because W795R Prom1
224 exhibited reduced EV formation and impaired trafficking to the plasma membrane, we hypothesized that
225 the mutation may alter cholesterol binding. To test this hypothesis, we developed a cholesterol
226 co-immunopurification assay (hereafter referred to as chol-IP) to quantify interaction of Prom1 with
227 fluorophore-labeled cholesterol (Fig 3A). Prom1-Strep was transfected into Expi293 cells, and cells were
228 labeled with a low concentration of fluorescent cholesterol. EVs were purified from the conditioned
229 media, solubilized with nonionic detergent (DDM), and immunoprecipitated with Strep resin trace labeled
230 with blue fluorescent protein (mTagBFP2-Strep). We then collected epifluorescence micrographs of the
231 resin particles, computationally segmented and filtered each image, and quantified bound cholesterol
232 using mTagBFP2 as a normalizing control (Fig 3A). This method allows for sensitive quantification of bound
233 lipid while efficiently excluding autofluorescent and refractive artifacts.

234

235 We purified BODIPY-cholesterol-labeled EVs produced by WT and mutant forms of Prom1 and subjected
236 equal input concentrations of Prom1 to chol-IP analysis. To our surprise, none of the mutants substantially
237 disrupted cholesterol binding, but the patient-derived W795R mutant and the two CARC domain mutants
238 bound cholesterol at higher levels than WT Prom1 (Fig 3B). To validate that differences in fluorescence
239 are indeed due to different quantities of bound cholesterol, we replicated the chol-IP assay with
240 AlexaFluor647-cholesterol for the W795R mutant and also observed an increase in cholesterol binding
241 relative to WT protein (Fig 3C). We conclude that W795R, CARC-1, and CARC-2 Prom1 are allosterically
242 biased toward a "cholesterol-locked" state that supports more stable cholesterol binding than the
243 distribution of states that WT Prom1 occupies. We chose to focus our efforts on the W795R mutant as it
244 is a naturally occurring single-residue mutation with exceptional evolutionary conservation and a clinically
245 validated disease phenotype.

To verify that W795R Prom1 does exhibit a gross oligomerization defect, we purified EVs from cells co-transfected with Strep-tagged and mScarlet-tagged Prom1 and measured co-purification of Prom1-mScarlet on Strep resin. Prom1 W795R co-purified with ~60% as much mScarlet fluorescence as WT Prom1, indicating that W795R indeed multimerizes, albeit with reduced efficiency (Fig 3D).

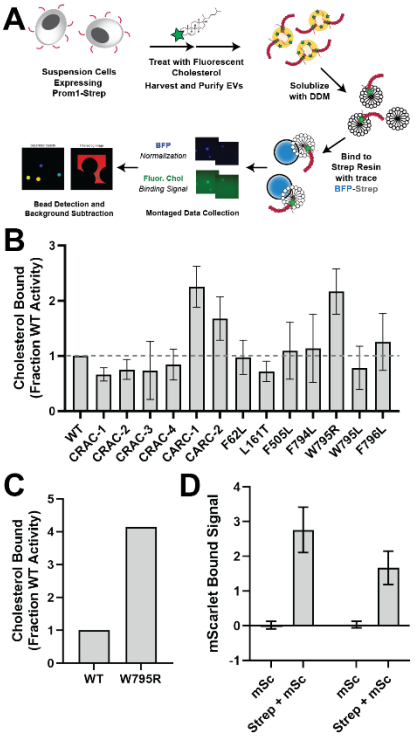

Figure 3. (A) Cholesterol co-immunoprecipitation (Chol-IP) assay graphic protocol. **(B)** BODIPY-cholesterol binding measurements for WT and mutant variants of Prom1. Error bars indicate S.D. (n = 3). **(C)** AlexaFluor647-cholesterol binding measurement for WT and W795R Prom1 **(D)** Red fluorescence signal from anti-Strep immunopurification of DDM-solubilized EVs from cells expressing Prom1-mScarlet ("mSc") or both Prom1-mScarlet and Prom1-Strep ("Strep + mSc"). Error bars indicate S.D. (n = 3).

Cholesterol binding is coupled to Prom1 N-glycosylation and maturation

We consistently observed that W795R Prom1 purified in EVs ran slightly faster on SDS-PAGE gels than WT Prom1 (Fig 4A). To determine whether *N*-glycosylation alone accounts for the difference in electrophoretic mobility, we treated WT and W795R Prom1 with PNGase F. Both Prom1 variants ran on gels at the same size after *N*-glycan removal, indicating that their native size difference is due to differential glycosylation (Fig 4A). Importantly, because Prom1 EVs form by blebbing from the plasma membrane, the EV material purified from cell-free conditioned media reflects the glycosylation state of

266 mature Prom1 from the plasma membrane rather than immature protein from the endomembrane
267 system.
268
269 We next tested whether *N*-glycosylation alters Prom1 cholesterol binding. We purified BODIPY-
270 cholesterol-labeled WT Prom1 EVs and incubated them with PNGase F to remove *N*-glycan moieties. Chol-
271 IP analysis indicated that *N*-glycan removal from mature Prom1 significantly increased the level of bound
272 BODIPY-cholesterol (Fig 4B). We similarly observed an increase in cholesterol binding for PNGase F-
273 treated EVs labeled with AlexaFluor647-cholesterol (Fig 4C).
274

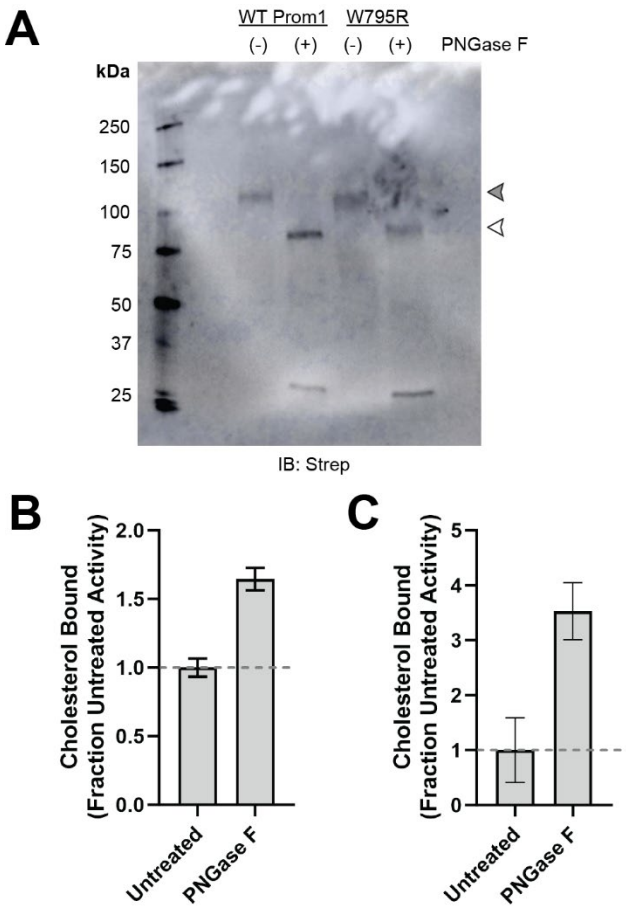

275

276 **Figure 4. (A)** Anti-strep immunoblot of denatured WT and W795R Prom1-Strep EVs treated with or
277 without PNGase F to remove *N*-glycosyl moieties. Filled and empty arrowheads indicate the expected
278 positions of fully glycosylated and deglycosylated Prom1-Strep, respectively. **(B)** Chol-IP measurement of
279 BODIPY-cholesterol binding in Prom1-Strep EVs treated with or without PNGase F. Error bars indicate
280 S.D. (n = 3). **(C)** Chol-IP measurement of AlexaFluor647-cholesterol binding in Prom1-Strep EVs treated
281 with or without PNGase F. Error bars indicate S.D. (n = 3).

282

283 *Prominin homolog Ttyh1 produces EVs but does not stably bind cholesterol*

284 Tweety homology (Ttyh) proteins are proposed prominin homologs that share the five-transmembrane
285 topology of prominins but have shorter extracellular domains (~120 amino acids in Ttyh vs ~280 amino
286 acids in Prom)[25] (Fig 5A). Given the shared evolutionary history of Prom and Ttyh, we hypothesized that
287 Ttyh may also bend membranes and produce EVs. Evolutionary analysis of metazoan Ttyh proteins does
288 not indicate conserved CRAC or CARC sites, nor does it suggest any conserved transmembrane residue
289 analogous to Trp-795 in metazoan prominins (Fig 5B).

290

291 We expressed Strep-tagged Ttyh1 in Expi293 cells and purified EVs using the same procedure as for Prom1
292 EVs (Fig 1A). We detected Ttyh1-Strep in CM, CCM, and SEC-purified EV fractions (Fig 5C). Dynamic light
293 scattering indicated that purified Ttyh1 EVs are monodisperse with an average diameter of 180 $\pm$ 10 nm,
294 similar to the average diameter of WT Prom1 EVs (164 ± 14 nm) (Fig 5D).

295

296 We next characterized the morphology of purified Ttyh1 EVs using NS-TEM. We found that Ttyh EVs
297 adopted striking long and bent tubular structures with much higher frequency than Prom1 EVs (6.4% of
298 Ttyh1 EVs versus 0.3% of Prom1 EVs, n = 1357 and n = 322 respectively) (Figs 5E, 5H). Ttyh1 EVs visualized
299 by NS-TEM were on average smaller than Prom1 EVs, and like Prom1 EVs were smaller than expected
300 from solution DLS measurement (Figs 5G, 5H). Furthermore, we observed that the smallest Ttyh1 EVs
301 were similar in diameter to the short-axis caliper diameter of the tubular EVs (42 ± 6 nm) and we observed
302 cases where tubular EVs appeared to be in the process of dividing into smaller EVs (Figs 5E, 5G). Although
303 the NS-TEM conditions deviate from a solvated physiological state, they do indicate that Ttyh1 supports
304 comparatively more bent membranes than Prom1.

305

306 We further analyzed Ttyh1 EVs by cryo-TEM to verify that the purified sample contained EVs. Indeed, we
307 observed vesicles with clear bilayer membrane density (Fig 5F). Like Prom1 EVs, Ttyh1 EVs have a bimodal
308 size distribution with local maxima around 60 nm and 140 nm (Fig 5G). We also observed a population of
309 EVs exhibiting the tubular phenotype seen in NS-TEM that again substantially exceeded that seen with
310 Prom1 EVs (8.8% of Ttyh1 EVs versus 0.8% of Prom1 EVs, n = 2224 and n = 176 respectively) (Fig 5H). This
311 supports the observation that the frequency of EV bending is more frequent in Ttyh1 EVs than Prom1 EVs.
312 We conclude that Ttyh1 supports greater membrane bending than Prom1, sufficient to induce
313 deformation and even membrane fission under NS-TEM and cryo-TEM conditions.

314

315 To further determine similarities and differences between purified Prom1 and Ttyh1 EVs, we subjected
316 purified EVs to equilibrium sucrose gradient sedimentation to resolve populations by density. We
317 observed a single population of Prom1 EVs (centered on fraction 7) but resolved two distinct populations
318 of Ttyh1 EVs with densities lower (centered on fraction 6) and higher (centered on fraction 9) than the
319 Prom1 EVs (Fig 5I). When Prom1 and Ttyh1 were co-expressed, we observed that the resulting EVs
320 followed the bimodal distribution of Ttyh1 EVs (Fig 5J). Immunoblots of the sucrose gradient fractions
321 showed that co-expressed Prom1 and Ttyh1 peak in the same sucrose gradient fractions, suggesting that
322 Prom1 and Ttyh1 co-elute in the same EV populations (Fig 5J, 5K). We conclude that Prom1 and Ttyh1
323 traffic to the same plasma membrane microdomains and can be secreted into the same EV membranes.
324
325 Finally, we compared stable cholesterol binding between Ttyh1 and Prom1 by purifying Ttyh1 EVs labeled
326 with BODIPY-cholesterol or AlexaFluor647-cholesterol and subjecting them to chol-IP analysis.
327 Surprisingly, neither cholesterol analog detectably co-purified with Ttyh1 (Figs 5L, S5). Taken together,
328 our observations suggest that Prom1 and Ttyh1 share evolutionary history and EV formation function but
329 differ in cholesterol interaction and the degree to which they support EV membrane bending.
330

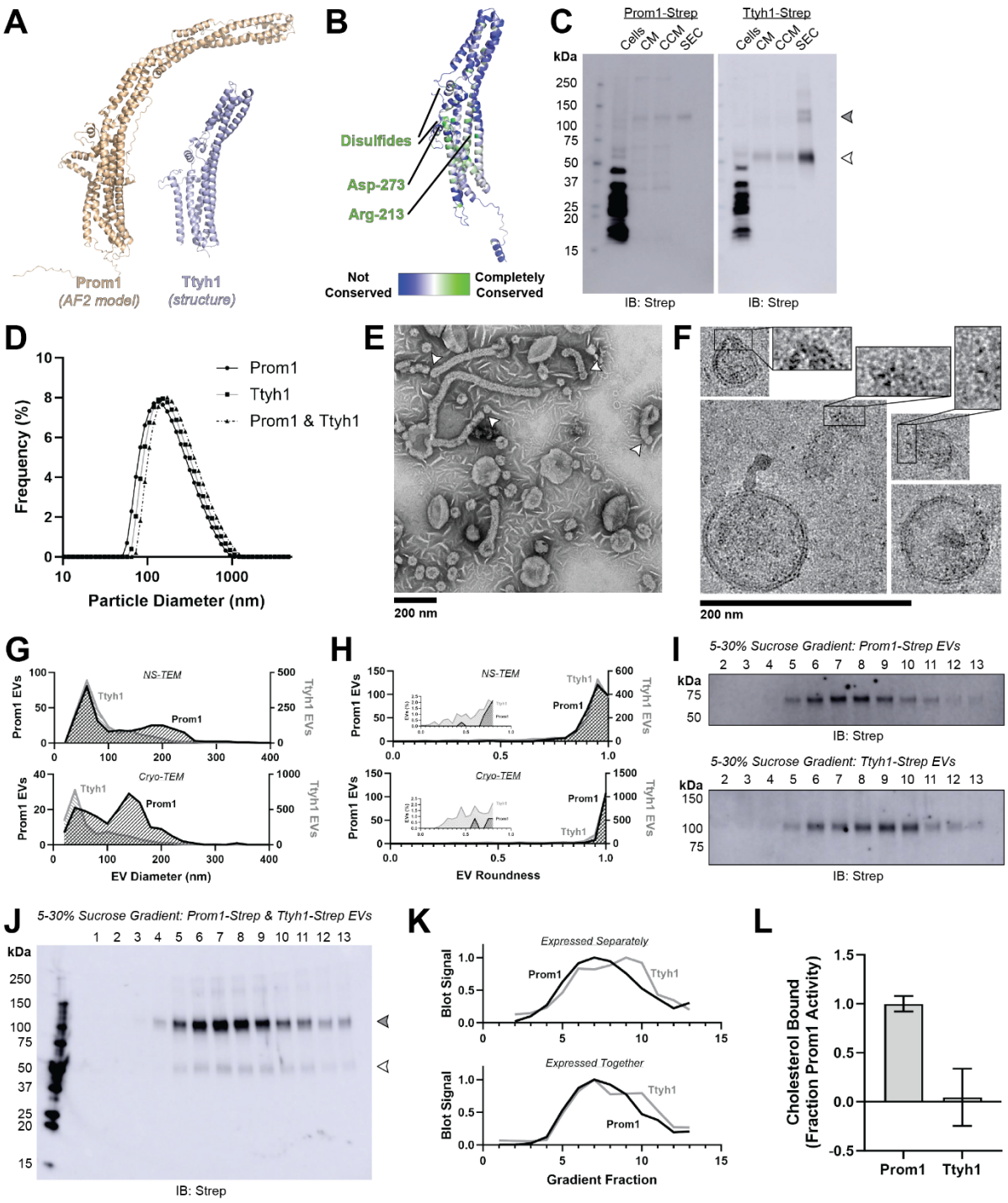

Figure 5. (A) Comparison of a Ttyh1 subunit from cryo-TEM structure 7P5J[37] with an AlphaFold2-predicted Prom1 monomer[46]. **(B)** Residue-level conservation among metazoan Ttyh proteins plotted onto a subunit of human Ttyh1. No residue analogous to Prom1 Trp-795 is present in Ttyh. **(C)** Anti-strep immunoblot comparing Prom1-Strep EVs and Ttyh1-Strep EVs throughout different stages of purification. Filled and empty arrowheads indicate the expected positions of Prom1 and Ttyh1,

338 respectively. Doublet and higher bands in Ttyh1 lanes are products of on-gel disulfide crosslinking in
339 concentrated samples. **(D)** Dynamic light scattering readouts for purified Prom1-Strep, Ttyh1-Strep, or
340 Prom1-Strep + Ttyh1-Strep co-expression EVs. **(E)** Representative NS-TEM images of Ttyh1-Strep EVs.
341 Arrowheads indicate possible sites of EV fission. **(F)** Representative cryo-TEM images of Ttyh1-Strep EVs.
342 Magnified insets show bilayer density at highly curved membrane segments. Images are lowpass filtered
343 to 5 Å to enhance contrast. **(G)** Comparison of Prom1 or Ttyh1 EV diameter in NS-TEM or cryo-TEM
344 images. (n = 322, n = 1357, n = 176, and n = 2224 for Prom1 NS-TEM, Ttyh1 NS-TEM, Prom1 cryo-TEM,
345 and Ttyh1 cryo-TEM measurements, respectively.) **(H)** Comparison of Prom1 or Ttyh1 EV roundness in
346 NS-TEM or cryo-TEM images. Inset plots only include EVs with roundness ≤ 0.8. (n = 322, n = 1357, n =
347 122, and n = 1546 for Prom1 NS-TEM, Ttyh1 NS-TEM, Prom1 cryo-TEM, and Ttyh1 cryo-TEM
348 measurements, respectively.) **(I)** Anti-strep immunoblots of fractions from sucrose gradient equilibrium
349 sedimentation of Prom1-Strep EVs (top) or Ttyh1-Strep EVs (bottom). **(J)** Anti-strep immunoblots of
350 fractions from sucrose gradient equilibrium sedimentation of EVs from cells co-expressing Prom1-Strep
351 and Ttyh1-Strep. Filled and empty arrowheads indicate the expected positions of Prom1 and Ttyh1,
352 respectively. **(K)** Quantification of immunoblots in panels *I* (top) and *J* (bottom). **(L)** Chol-IP
353 measurement of cholesterol binding in Prom1-Strep or Ttyh1-Strep EVs. Error bars indicate S.D. (n = 3).

354

355 *Prom1 W795R EVs are morphologically similar to WT Prom1 EVs*

356 Because Ttyh1 stabilizes greater membrane curvature than Prom1 but does not stably bind cholesterol,
357 we hypothesized that cholesterol binding may negatively regulate membrane bending by prominin-family
358 proteins. This model predicts that W795R Prom1, which binds cholesterol more stably than WT protein,
359 should not produce EVs that exhibit the tubular morphology observed in Ttyh1 EVs. When measured by
360 DLS, we observed a similar solution size for WT (164 ± 14 nm) and W795R EVs (186 ± 13 nm) (Figs 2D, 6A).
361 We measured the size and shape of W795R EVs by cryo-TEM and observed largely spherical vesicles with
362 some local deformations, similar to what we observed with WT Prom1 EVs (Fig 6B). Generally, WT and
363 W795R Prom1 EVs have similar roundness profiles, with W795R having no vesicles that fall into our tubular
364 morphology classification (n = 1211) (Fig 6C). Though both large and small diameter EV populations were
365 observed by cryo-TEM, W795R Prom1 had a larger fraction of small EVs than WT Prom1, indicating
366 possible decreased stability or increased fissile propensity in the W795R Prom1 EVs (Fig 6D).

367

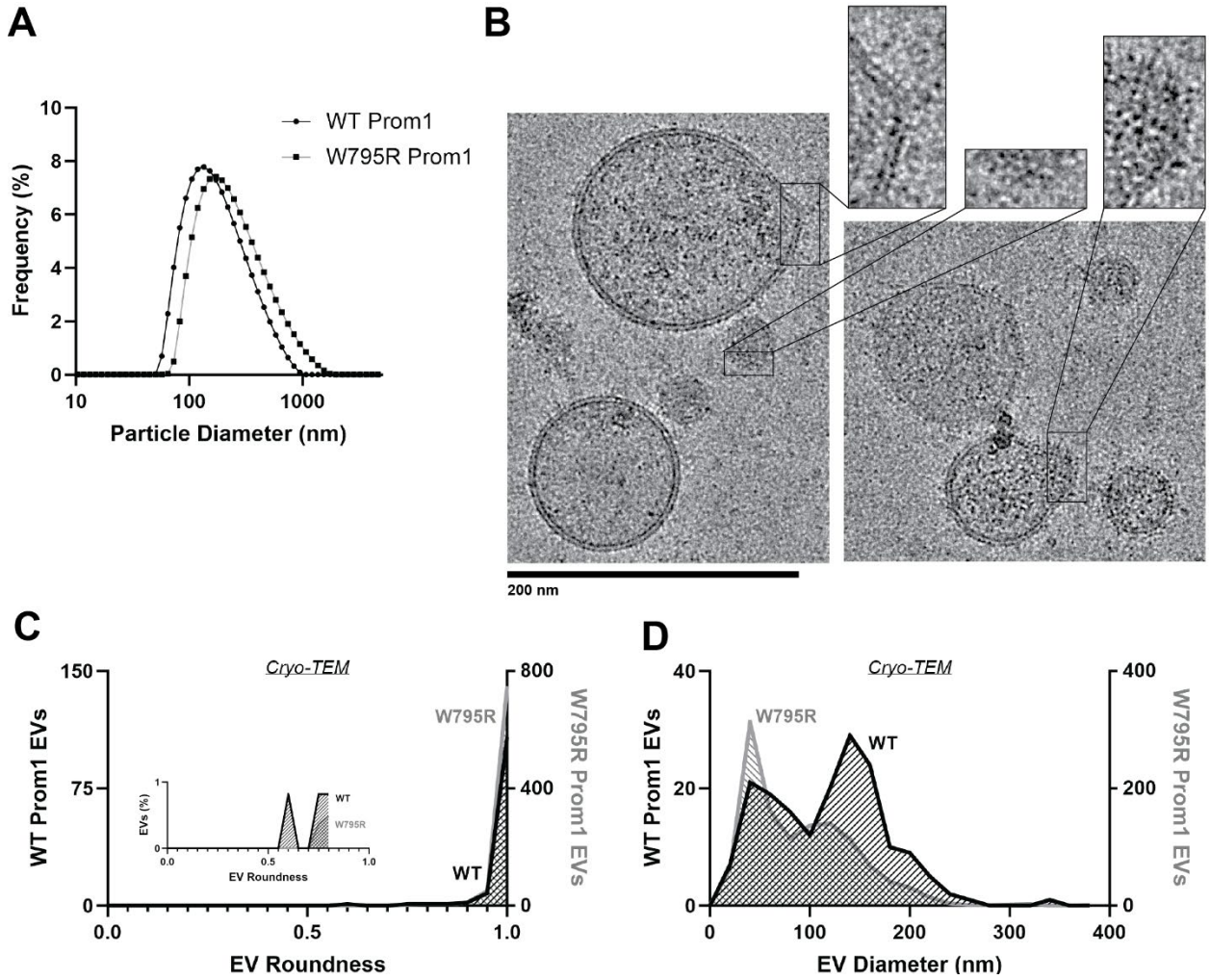

Figure 6. (A) Dynamic light scattering readouts for purified WT or W795R Prom1-Strep EVs. **(B)** Representative cryo-TEM images of W795R Prom1-Strep EVs. Magnified insets show bilayer density. Images are lowpass filtered to 5 Å to enhance contrast. **(C)** Comparison of WT or W795R EV roundness in cryo-TEM images. Inset plots only include EVs with roundness ≤ 0.8. (n= 176 and n = 1211 for WT and W795R Prom1 cryo-TEM measurements, respectively.) **(D)** Comparison of WT or W795R Prom1 EV diameter in cryo-TEM images. (n= 122 and n = 821 for WT and W795R Prom1 cryo-TEM measurements, respectively.)

Cholesterol binding modulates membrane bending by Prom1

A further prediction of the model that cholesterol binding negatively regulates membrane bending is that depleting cholesterol from EV membranes could induce a Ttyh1-like morphology in Prom1 EVs. We tested this model directly by purifying WT Prom1 or Ttyh1 EVs and treating them with methyl beta cyclodextrin (mBCD), a compound that extracts cholesterol from membranes[26,47]. After re-purifying EV samples away from free mBCD and mBCD-cholesterol complexes, Prom1 and Ttyh1 EVs treated with mBCD (2.5-10 mM)

383 exhibited a decrease in cholesterol content (Fig 7A). At increasing concentrations of mBCD, we observed
384 depletion of Prom1 and Ttyh1 after EV re-purification, suggesting that cholesterol depletion may
385 destabilize EVs (Fig 7B). Treated and untreated EVs were then analyzed by NS-TEM to compare EV size
386 and morphology (Fig 7C). We observed a 5.4-fold increase in the fraction of Prom1 EVs that deviated from
387 spherical membrane topology after 10 mM mBCD treatment compared to untreated EVs (3.0% versus
388 0.6% of EVs, n = 232 and n = 356 respectively) (Fig 7D). In contrast, Ttyh1 EVs treated with mBCD under
389 identical conditions only showed a 1.4-fold increase in deformed EVs (2.1% versus 1.5% of EVs, n = 433
390 and n = 535 respectively) (Fig 7D). This indicates that EV membrane deformation is specific to Prom1 EVs
391 rather than a nonspecific effect triggered by EV cholesterol depletion. Thus, cholesterol-depleted Prom1
392 mimics the membrane bending activity of Ttyh1.
393

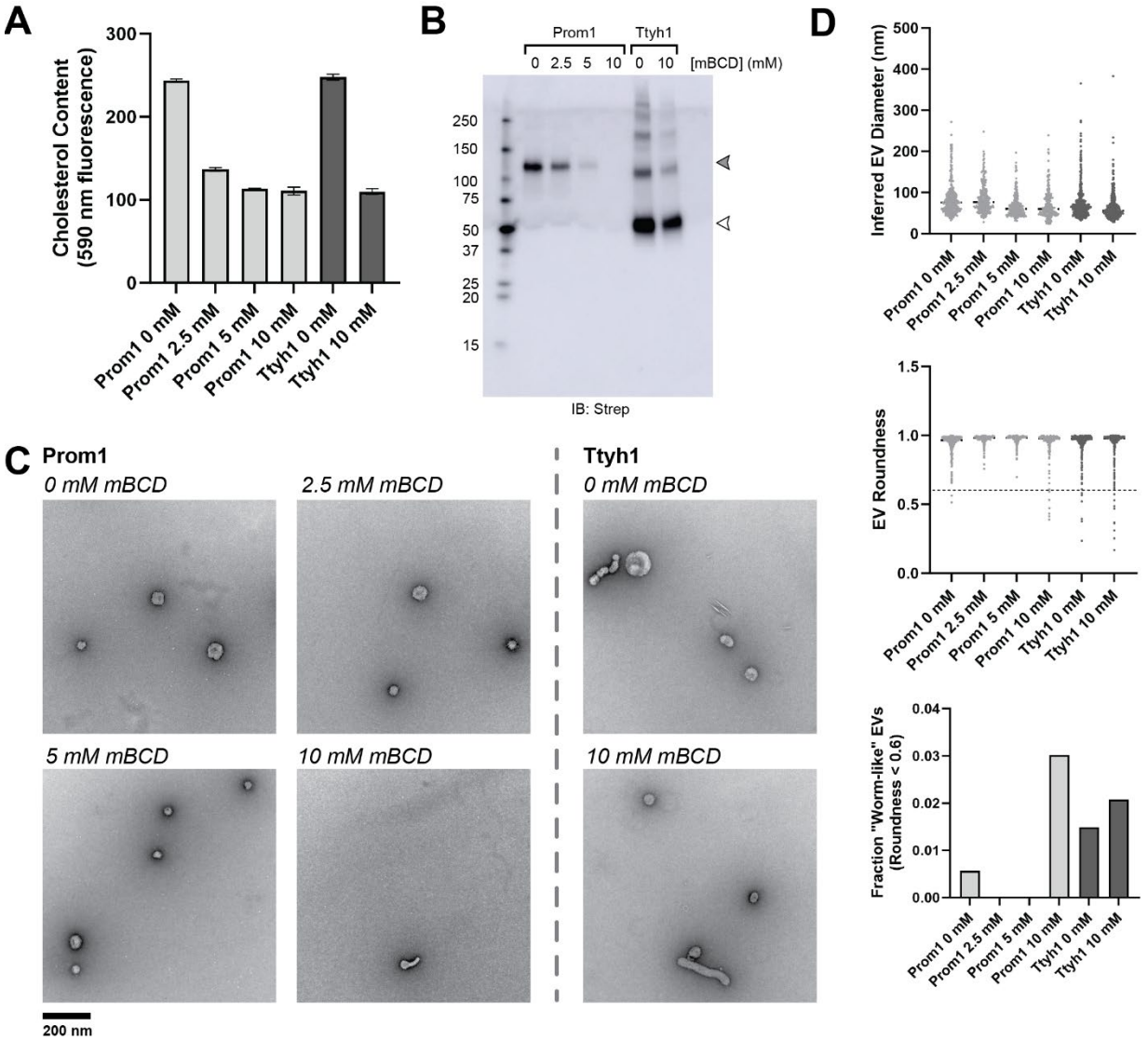

394

395 **Figure 7. (A)** Cholesterol content of Prom1 or Ttyh1 purified EV samples after treatment with mBCD.
396 Error bars indicate S.D. (n = 3). **(B)** Anti-strep immunoblot of mBCD-treated and purified Prom1 or Ttyh1
397 EVs. Filled and empty arrowheads indicate the expected positions of Prom1 and Ttyh1, respectively.
398 Higher-MW bands are products of on-gel disulfide crosslinking. **(C)** Representative NS-TEM images of
399 mBCD-treated and purified EVs. **(D)** Quantification of EV diameter (*top*) and roundness (*middle*) from
400 NS-TEM images, as well as quantification of EVs with roundness < 0.6 (*bottom*).

401

402 **Discussion**

403 *Prominin-family proteins Prom1 and Ttyh1 bend membranes and form EVs*

404 Prominin and Tweety homology proteins are both biologically implicated in membrane bending processes.
405 Prominins localize to cholesterol-rich microdomains of the plasma membrane and drive protrusion-shed
406 EV formation in differentiating stem cells[26–28]. Tweety homology proteins are associated with dendritic
407 spikes in healthy neurons and with tumor microtube formation in aggressive astrocytoma[32,39–41]. We
408 report here that both Prom1 and Ttyh1 can induce EV secretion from cultured cells upon overexpression
409 (Fig 5C). Though we do not claim that Ttyh1 endogenously induces EV formation, we note that it is
410 sufficient to do so in a recombinant system with similar efficiency to Prom1. Given similar membrane
411 remodeling tubulation behavior of Prom1 and Ttyh1 in cell culture[25,40], Ttyh1 EVs may form by a similar
412 mechanism to Prom1 EV formation.

413

414 We find that Prom1 and Ttyh1 form EVs that are of similar size, and that the two proteins exist in the same
415 pool of EVs when co-expressed in cell culture (Figs 5J, 5K). Because Prom1 EVs arise directly from blebbing
416 of the plasma membrane, this finding suggests that Prom1 and Ttyh1 traffic endogenously to the same
417 lipid microdomains. Given their similarities in localization, membrane bending behavior, and
418 transmembrane topology, we propose that Prominins and Tweety homology proteins be considered
419 members of a broader prominin family of membrane remodeling proteins.

420

421 Membrane bending by Prom1 is critical for maintaining homeostasis in photoreceptor outer segments.
422 Intriguingly, photoreceptors with impaired expression of the disc rim stabilizing protein Peripherin
423 accumulate EVs 200-280 nm in diameter at the outer segment base[48]. Intriguingly, we observe formation
424 of Prom1 EVs of relatively similar size in our reconstituted system (Fig 1D). This may be an example of
425 endogenous regulation of Prom1-induced membrane curvature, with curvature-stabilizing proteins like
426 peripherin preventing the evaginating membrane from budding into EVs.

427

428 *Cholesterol binding regulates membrane bending by Prom1, but not Ttyh1*

429 We find here that Prom1 in EVs forms a stable interaction with cholesterol that is resistant to delipidation
430 by nonionic detergent (Fig 3B). By contrast, Ttyh1 does not stably bind cholesterol (Fig 5L). Though both
431 proteins induce release of similarly sized EVs, Prom1 EVs appear predominantly spherical when visualized
432 by NS-TEM whereas a substantial fraction of Ttyh1 EVs appear tubular and rearrange into smaller EVs (Figs
433 1G, 5E). Prom1 EVs mimic the Ttyh1-like deformed morphology when cholesterol is depleted from EV
434 membranes, indicating that cholesterol interaction negatively regulates membrane bending by Prom1
435 (Figs 7C, 7D).

436

437 A disease-associated mutation in a strikingly conserved residue in the fifth transmembrane helix of Prom1,
438 W795R, substantially stabilizes cholesterol binding (Figs 2A, 3B). In AlphaFold2 models, Trp-795 forms a
439 series of base-stacking interactions with Phe residues in neighboring transmembrane helices (Fig 2B)[46].
440 We find that conservative mutations in several of these adjacent aromatic residues impair EV formation
441 by Prom1, but do not mimic the stable cholesterol binding of W795R (Figs 2C, 3B). In a comparison of the
442 two lowest-energy AlphaFold2 dimer models of Prom1, the conformation of this aromatic core remains
443 constant despite a global change in Prom1 topology (Figs 8A, S6B). This suggests that neither predicted
444 Prom1 dimer reveals a potential cholesterol-locked conformation adopted by W795R Prom1. Cholesterol
445 is asymmetrically distributed in eukaryotic membranes, with a bias toward the outer leaflet of the plasma
446 membrane[49]. Prom1 Trp-795 is also predicted to be positioned toward the outer leaflet, possibly
447 potentiating its cholesterol interactions. We also observe increases in cholesterol binding stability for
448 mutations to two CARC domains in Prom1 (Fig 3B). This effect could arise because these residues interface
449 with cholesterol or destabilize the transmembrane domain in a manner that mimics the effect of the
450 W795R mutation. Given the poor evolutionary conservation of the two CARC motifs in human Prom1, we
451 favor the latter explanation.

452

453 We further show that the W795R mutation prevents efficient trafficking and plasma membrane insertion
454 of Prom1 from the endomembrane to the plasma membrane (Figs 2E, 2F). This observation explains the
455 very low yield of W795R EVs produced in cell culture. W795R Prom1 was well expressed but strongly
456 localized to WGA^+ intracellular vesicles. These vesicles are believed to traffic downstream of the trans-
457 Golgi, suggesting that the roadblock in W795R Prom1 endomembrane trafficking occurs between the
458 trans-Golgi and the plasma membrane[50]. Dynamic cholesterol interaction and conformational changes
459 may be required for proper maturation and trafficking of Prom1 within the endomembrane system. The

460 altered *N*-glycan profile of W795R may also contribute to this effect, as ablation of genes involved in *N*-
461 glycan biosynthesis inhibits Prom1 trafficking to the plasma membrane[51] (Fig 4A).
462
463

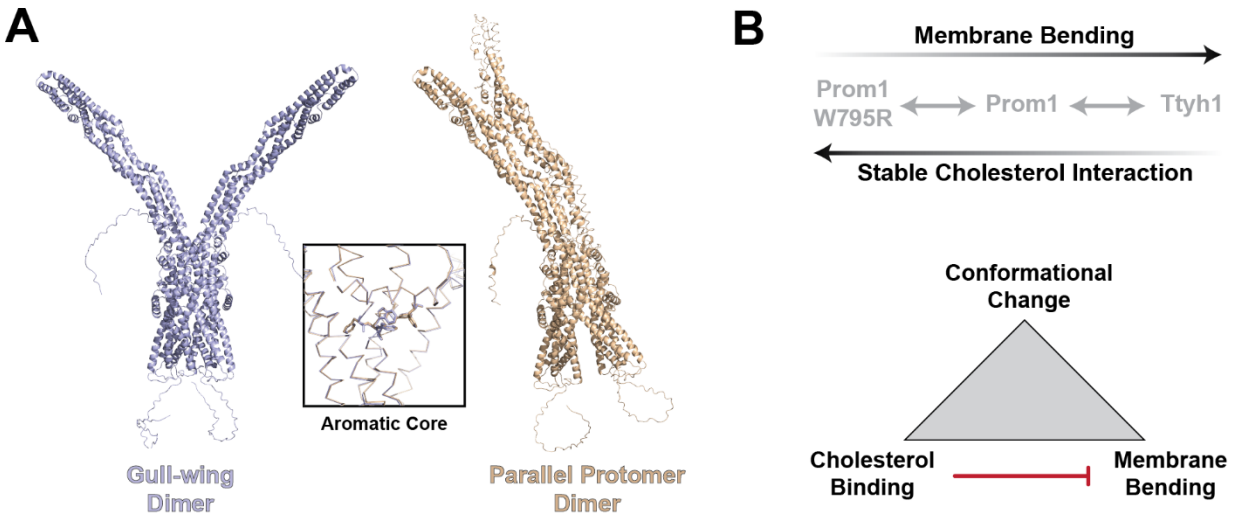

464
465

466 **Figure 8. (A)** Comparison of highest-ranked AlphaFold2 dimer models of Prom1[46]. Inset shows an
467 alignment of the core aromatic cluster (Phe-62, Phe-505, Phe-794, Trp-795, Phe-796) between the two
468 models indicating the highly consistent transmembrane domain prediction. **(B)** Model for coupled
469 conformational change, cholesterol interaction, and membrane bending in prominin-family proteins.

470

471 *N-glycosylation is necessary for Prom1 function*

472 Many membrane proteins are *N*-glycosylated in the endoplasmic reticulum, and *N*-glycans are further
473 modified in the Golgi[52]. Prom1 is no exception, with eight predicted *N*-glycosylation sites in the large
474 extracellular loops[7,51]. Each site is individually dispensable for Prom1 trafficking to the plasma membrane,
475 but complete ablation of glycosylation disrupts trafficking[51]. We find that the *N*-glycan moieties on Prom1
476 are not only required for maturation and trafficking, but also destabilize Prom1-cholesterol interaction
477 (Fig 4B). A previous study has reported that mature Prom1 can exist in complex or high-mannose
478 glycosylation profiles that have distinct interaction profiles with other proteins at the plasma membrane[10].
479 Though our system cannot directly dissect the relationship between different *N*-glycosylation profiles and
480 Prom1 conformation, we do note that mutations in Trp-795 appear to bias Prom1 away from complex
481 glycosylation and toward a lower molecular weight product consistent with a high-mannose profile (Fig
482 4A). It is therefore possible that regulated *N*-glycosylation functionalizes Prom1 for different roles within

483 different tissues by altering interaction with cholesterol and the degree of membrane bending that the
484 protein supports.
485
486 *Prom1 cholesterol binding regulates membrane bending*
487 We propose here that Prom1 forms dynamic interactions with cholesterol that contribute to regulation
488 of membrane bending (Fig 8B). These cholesterol-dependent interactions allosterically modulate Prom1
489 and are functionally linked to the glycosylation state of the protein. It is important to note that the
490 cholesterol function at the plasma membrane is highly pleiotropic. Cholesterol contributes to membrane
491 remodeling specifically through allosteric modulation of prominins and nonspecifically through lipid
492 microdomain organization and modulation of membrane fluidity.
493
494 The Prom1 homolog Ttyh1 lacks stable interaction with cholesterol, has no conserved analog of the Trp-
495 795 residue, and supports greater membrane deformation than WT Prom1. Though Ttyh proteins are
496 evolutionarily divergent from Prom proteins and the explanations for their different membrane bending
497 behavior are likely multifaceted, we find the ability of Prom1 to mimic Ttyh1 activity upon cholesterol
498 depletion notable. Prominins may therefore be regulated membrane benders that can fulfill different
499 roles in different tissue types, whereas Ttyh proteins are constitutive membrane benders exclusively
500 expressed in neuronal niches that require this function. Further study of regulated prominin-family
501 function in different tissue contexts will be necessary to fully understand the role of prominin-dependent
502 membrane remodeling in cellular function.
503
504 **Materials and Methods**
505 *Expression Constructs*
506 All Prom1 expression constructs were generated by site-directed mutagenesis from pCS2-Prom1-YFP (a
507 generous gift from N. Sasai, Nara Institute of Science and Technology). The base Prom1 construct used is
508 the human S1 isoform (NCBI accession NP_001139319.1)[53]. Prom1-Strep was subcloned into pLV-EF1a
509 vector (a generous gift from K. Hochedlinger, Massachusetts General Hospital) for lentiviral transduction.
510 Human Pcdh21 isoform 1 (NCBI accession NP_149091.1) was synthesized (GenScript) and cloned into a
511 pCDNA3.1 vector (ThermoFisher) for mammalian cell transfection. mTagBFP2 was subcloned from pBAD
512 (Addgene #54572, a gift from Michael Davidson) into a pET28a vector with a C-terminal Strep tag for
513 bacterial overexpression. Ttyh1 was expressed from a pLX304 vector after addition of C-terminal Strep
514 and His tags to an existing construct (Addgene #161676, a gift from Mike McManus). To stably express

515 fluorescently tagged Prom1 WT and W795R variants in HeLa cells for live cell imaging, Prom1-StayGold
516 and Prom1[W795R]-StayGold sequences were synthesized (GenScript) and cloned into P2555 vector (kind
517 gift by S. Jakobs, Max Planck Institute for Biophysical Chemistry) to yield constructs pAH18 and pAH20,
518 respectively.
519
520 *Cell Line Construction*
521 Cell lines were regularly tested for mycoplasma contamination. Lentiviral transduction of Prom1-Strep
522 into Expi293 cells was performed using a modification of published protocols[54,55]. Briefly, lentiviral
523 particles were produced in 293T cells (ATCC) by transient transfection of pLV-EF1a-Prom1-Strep with
524 VSVG and Delta 8.9 plasmids (a generous gift from K. Hochedlinger, Massachusetts General Hospital) using
525 the Lipofectamine 3000 system (Thermo Fisher) and incubated overnight at 37 °C, 5% CO_2. Expi293 cells
526 (Thermo Fisher) raised for several passages in suspension culture were seeded onto adherent tissue
527 culture plates in adherent culture media (DMEM (Gibco) supplemented with 10% Fetal Bovine Serum
528 (Gibco) and 1x Penicillin/Streptomycin (Gibco)) and incubated overnight at 37 °C, 5% CO_2 to form an
529 adherent monolayer. Transfected cells were exchanged into fresh adherent culture media. Culture media
530 was harvested after an additional 48 h, filtered through a 0.45 µm vacuum unit, and concentrated from
531 70 mL to 0.3 mL in PBS buffer by ultracentrifugation according to established protocols[55]. Adherent
532 Expi293 cells were infected with concentrated lentiviral particles at 75% confluency in adherent culture
533 media supplemented with 8 µg/mL polybrene (Sigma-Aldrich), then incubated for 48 h at 37 °C, 5% CO_2.
534 Cells were gently washed with PBS, exchanged into adherent culture media, and incubated for 24 h at
535 37 °C, 5% CO_2. Subsequently, the cells were subjected to antibiotic selection by exchange into adherent
536 culture media containing 2 µg/mL Blasticidin (Gibco) for 10 days with regular exchange into fresh selective
537 media and passaging to prevent cells from achieving full confluency. Selection was considered complete
538 when the majority of cells died and antibiotic-resistant foci recolonized the culture plate. The cells were
539 then trypsinized (Gibco) and transitioned back to suspension culture in modified suspension culture media
540 (Expi293 media (Gibco) supplemented with 1% Fetal Bovine Serum) at a density of 1.0 x 10^6 live cells per
541 mL of culture and incubated for 48 h at 37 °C, 8% CO_2 with 125 rpm rotation. Once the suspension culture
542 reached a density of 3.0 x 10^6 live cells per mL of culture, cells were re-passaged in 1.0 x 10^6 live cells per
543 mL of culture in fresh modified suspension culture media supplemented with 1.5 µg/mL Blasticidin, and
544 subsequently re-passaged into this media condition every 2 days.
545

546 For generation of stable HeLa cells expressing WT Prom1-StayGold and Prom1[W795R]-StayGold off the
547 AAVS1 site, the donor plasmids pAH18 or pAH20 were co-transfected with the nuclease plasmid PX458-
548 AAVS1 (kind gift by S. Jakobs, Max Planck Institute for Biophysical Chemistry) using Lipofectamine 3000
549 (Thermo Fisher Scientific). Transfected cells were selected with 10 µg/mL blasticidin (Gibco) starting 48 h
550 post-transfection for 7 days. Stable clones were expanded for 10 days, and single-cell GRP-positive clones
551 were obtained using a FACS AriaII Cell Sorter (BD Biosciences). After clonal expansion, positive clones were
552 detected and verified by fluorescence imaging.
553
554 *Synthesis of fluorescent cholesterol analogs*
555 BODIPY-cholesterol was procured commercially (TopFluor cholesterol, Avanti Polar Lipids) and
556 resuspended at 1 mM in ethanol. AlexaFluor647-cholesterol was synthesized from Alkyne Cholesterol and
557 AZDye 647 Azide Plus (Click Chemistry Tools). Briefly, 1 mM AZDye 647 Azide Plus and 2 mM alkyne
558 cholesterol (each from a 10 mM stock prepared in anhydrous DMSO) were combined with 2 mM
559 tetrakis(acetonitrile)copper(I) tetrafluoroborate (from a 40 mM stock prepared in ethanol) in a 350 µL
560 reaction brought up to volume with ethanol. The reaction was incubated at 42 °C for 30 min then at 70 °C
561 for 2 h with the reaction vessel open to allow solvent to evaporate. Cholesterol was extracted from the
562 final mixture by diluting the solution to 650 µL with PBS buffer and adding 1 mL methanol and 0.5 mL
563 chloroform. The mixture was centrifuged for 2 min at 14,000 x *g* and the supernatant transferred to a
564 clean vessel, after which 1 mL of chloroform and 2 mL of glacial acetic acid were added and mixed by
565 vortexing. The solution was then concentrated by evaporation in a SPD1010 SpeedVac instrument
566 (Savant) until dried, then resuspended in 100 µL ethanol. This preparation was considered to be at 5 mM
567 labeled cholesterol (assuming 100% yield) for downstream calculations.
568
569 *Prom1 and Ttyh1 EV Reconstitution*
570 Prom1 and Ttyh1 EVs were reconstituted by expression in Expi293 suspension cells. Briefly, Expi293 cells
571 grown in serum-free Expi293 media at 37 °C, 8% CO_2 with 125 rpm rotation to a density of 3.0 x 10^6 live
572 cells per mL of culture were transiently transfected with an appropriate plasmid at 1 µg of DNA per 1 mL
573 of culture using the Expifectamine transfection kit (Thermo Fisher) according to the manufacturer
574 protocol. After 48 h, cultures were centrifuged for 5 min at 500 x *g*, the media discarded, and the cells
575 resuspended in the same volume of fresh Expi293 media and returned to incubate for an additional 48 h.
576 After this final incubation, cultures were centrifuged for 5 min at 1500 x *g* and the conditioned media
577 transferred to clean 50 mL conical tubes.

578

579 EVs labeled with fluorescent cholesterol analogs were generated as described above with the following
580 modifications. Two days after transfection, cells were transferred to 50 mL conical tubes, centrifuged for
581 5 min at 500 x *g*, then resuspended in an equal volume of Expi293 media with fluorescent cholesterol
582 added to a final concentration of 1 µM. Cells were transferred back to shaker flasks and incubated for 24
583 h before conditioned media was harvested.

584

585 *EV Purification*

586 Conditioned media was clarified immediately after harvest by centrifuging for 30 min, 10,000 x *g* at 4 °C;
587 then transferring the supernatant to clean tubes and centrifuging again for 1 h, 21,100 x *g* at 4 °C. The
588 supernatant was transferred to clean 50 mL conical tubes and stored at 4 °C until ready for further
589 purification. Clarified conditioned media was transferred to Seton 7030 tubes and each tube underlaid
590 with a 100 µL cushion of 50% sucrose. Tubes were centrifuged in an SW-41 Ti rotor (Beckman Coulter) for
591 1 h, 36,000 rpm at 4 °C, then ≥ 200 µL of volume was harvested from the bottom of each tube. In cases
592 where the total harvested volume exceeded 500 µL, the harvested volume was diluted to 11 mL with
593 sterile-filtered PBS buffer, transferred to a final Seton 7030 tube, underlaid with a 100 µL cushion of 50%
594 sucrose, re-centrifuged as described above, and 500 µL of volume harvested from the bottom of the tube.
595 Concentrated EVs were then purified by size exclusion chromatography into sterile-filtered PBS buffer
596 using qEV2-35 nm gravity columns (Izon) at ambient temperature (0.5 mL load volume, 2.5 mL void
597 volume, 1.2 mL harvest volume). Purified EVs were stored at 4 °C for up to 8 weeks, over which time no
598 evidence of Prom1 degradation was observed.

599

600 *Immunoblots*

601 Protein samples were run on 4-20% or 7.5% Mini-PROTEAN TGX SDS-PAGE gels (BioRad), then transferred
602 to PVDF membranes using the TurboBlot semi-dry transfer system (BioRad). Blots were washed briefly 3
603 times with 10 mL of PBST buffer, then incubated for 1-2 h at room temperature in PBST with blocking
604 agent (5 mg/mL Bovine Serum Albumin (Sigma Aldrich) for anti-Strep blots, 5% nonfat dry milk for all other
605 blots). Blocking solution was removed and primary antibody solution in PBST with blocking agent (1:2000
606 rabbit anti-Strep (Abcam #76949), 1:4000 mouse anti-Flag (Millipore Sigma #F3165), 1:2500 mouse
607 AC133-1 (Miltenyi #130-111-756)) for 2 h at ambient temperature or for 12-72 h at 4 °C. The blots were
608 then washed 3 times for 5-10 min with 10 mL PBST. Secondary antibody solution (1:5000 ECL anti-Mouse
609 (Cytiva) or 1:10,000 ECL anti-Rabbit (Cytiva)) in PBST with appropriate blocking agent was then added to

610 the blots and incubated for 1 h at ambient temperature. Blots were incubated with 5 mL Western Lighting
611 ECL solution (PerkinElmer) for 1 min and imaged using the chemiluminescence setting on an Amersham
612 680 gel imager (GE Healthcare). Blots were adjusted for brightness and contrast using GIMP (GNU Project)
613 and annotated with Illustrator (Adobe).
614
615 *Immunoblot Quantification*
616 Samples were treated first with 250 U PNGase F (New England Biolabs) for 2 hr at 37 °C to condense each
617 protein to a single molecular weight, then with 4 mM N-propyl maleimide (Millipore Sigma) for 1-2 h at
618 37 °C to block reactive cysteines and prevent on-gel disulfide crosslinking. Reactions were quenched by
619 addition of reducing SDS-PAGE loading buffer. After blotting and imaging, images were adjusted for
620 brightness and contrast and subjected to digital densitometry with ImageJ[56]. Resulting measurements
621 were reported normalized to WT Prom1 on each blot to allow comparisons between blots.
622
623 *Dynamic Light Scattering*
624 Dynamic light scattering (DLS) measurements were performed using an SZ-100 Nano Particle Analyzer
625 (Horiba). EVs diluted in PBS to a volume of 1 mL were transferred to a disposable plastic cuvette (Fisher)
626 and measurements were taken using settings for polydisperse liposomes in aqueous buffer. All
627 measurements were taken at 25 °C in multiple technical replicates to control for instrument sampling
628 error.
629
630 *Glycosylation Assays*
631 PNGase F (New England Biolabs) was used to remove *N*-glycan moieties from proteins. For *N*-glycan
632 removal under denaturing conditions, the PNGase F kit was used as directed. For *N*-glycan removal under
633 native conditions, 250 U of PNGase F enzyme were added to EVs in PBS buffer in a 25 µL reaction, then
634 incubated for 2 h at 37 °C.
635
636 *Silver stain*
637 EV samples were run on 7.5% SDS-PAGE Tris-Glycine gels and stained with Pierce Silver Stain for Mass
638 Spectrometry (Thermo Scientific) according to the manufacturer's protocol.
639
640 *Cryo-TEM Sample Preparation and Imaging*

641 Prom1 and Ttyh1 EVs were vitrified on 300-mesh gold Quantifoil R 1.2/1.3 + 2 nm Carbon grids (Electron
642 Microscopy Sciences). Briefly, grids were glow discharged in an EasiGlow device (Pelco) set to 5 mA, 30 s,
643 0.39 mbar, with a 15 s vacuum hold time. The grids were then treated with 5 µL of purified EVs, incubated
644 for 60 s to allow EVs to adhere to the carbon layer, then blotted with a VitroBot Mark IV (Thermo Scientific)
645 set to 22 °C, 5 s blot time, +15 blot force, 100% humidity; and plunge frozen in liquid ethane. Vitrified
646 samples were imaged on a Titan Krios microscope (Thermo Scientific) with a Falcon 4 direct electron
647 detector (Thermo Scientific) using counted detection mode, 105,000 x nominal magnification, 0.83 Å pixel
648 size, with 49-frame fractionated collection, 49.8 $e^-/Å^2$ total dose, and defocus ranging from -0.8 to -2.0
649 µm in 0.1 µm increments. Images were processed and analyzed with CryoSparc v. 4.2.1 (Stuctura
650 Biotechnology). Vesicles were defined and diameter (all EVs) and roundness (only EVs completely visible
651 on one micrograph) were calculated using custom scripts that extend CryoSparc, made publicly available
652 at https://github.com/tribell4310/vesicle-quantification.
653
654 *NS-TEM Sample Preparation and Imaging*
655 Formvar carbon film 400-mesh copper grids (Electron Microscopy Sciences) were glow discharged in an
656 EasiGlow device (Pelco) set to 30 mA, 30 s, 0.39 mbar, with a 15 s vacuum hold time. 5 µL of EV sample
657 was applied to a glow-discharged grid and incubated for 60 s at room temperature. The grid was then
658 blotted manually with filter paper (Whatman #43), briefly washed 3 times with 20 µL of PBS buffer,
659 blotted, washed 2 times with deionized water, blotted, washed 1 time with 1.25% (w/v) uranyl formate
660 (Electron Microscopy Sciences), and blotted. The grid was then floated for 10 s on a 20 µL of drop of 1.25%
661 uranyl formate, blotted, and allowed to air dry. Imaging was performed on a Tecnai T12 transmission
662 electron microscope (FEI) equipped with an XR16 detector (AMT) operated at an accelerating voltage of
663 120 kV, 30,000 x nominal magnification, 4.32 Å pixel size, and -1.5 µm defocus. Pixel size was manually
664 calibrated prior to image acquisition using a dedicated calibration waffle grid (Ted Pella). Vesicles were
665 defined and analyzed as described in CryoSparc (Structura Biotechnology) as described above for cryo-
666 TEM data.
667
668 *Evolutionary Analysis of Prom and Ttyh proteins*
669 We identified sequences homologous to human Prom1 using BLAST[57] and InterPro[58]. Putative prominin
670 sequences were curated to include only sequences with five predicted transmembrane helices by
671 TMHMM[59] in a 2+2+1 pattern, containing large extracellular loops (> 300 amino acids) and 2 small
672 intracellular loops (< 25 amino acids). This broad search revealed prominin sequences across the

673 eukaryotic tree ranging from metazoans to green plants. Multiple sequence alignment was performed
674 using MAFFT[60] and phylogenetic relationships inferred using IQ-TREE with MODELFIND for evolutionary
675 model selection[61,62]. Branch supports were calculated using the approximate likelihood ratio test[63]. A
676 smaller tree was also constructed spanning only metazoan sequences, with fungi included as an outgroup
677 for rooting. For direct comparison between Prom and Ttyh sequences, homologs of human Ttyh1 were
678 identified for all species included in the prominin metazoan tree and aligned as described above. Figures
679 showing multiple sequence alignments were generated using JalView[64]. Figures showing trees were
680 generated using IcyTree[65].
681
682 Conservation of each residue within the Prom and Ttyh metazoan trees was calculated using the
683 Livingstone and Barton algorithm implemented in JalView[66]. Conservation scores were then plotted onto
684 the AlphaFold2 structure model[46] of human Prom1 or a subunit of the solved cryo-EM structure of human
685 Ttyh1[37] using PyMol (Schrödinger).
686
687 *Live Cell Fluorescence Microscopy and Analysis*
688 Confluent monoclonal HeLa cells stably expressing WT Prom1-StayGold and Prom1[W795R]-StayGold
689 were harvested, seeded onto 35 mm glass-bottom dishes (MatTek Life Sciences) coated with poly-D-lysine
690 (0.1 mg/mL) and allowed to grow overnight at 37˚C under 5% CO_2. Cells were stained with wheat germ
691 agglutinin (WGA) conjugated with Alexa Fluor 647 (W32466, Thermo Fisher Scientific) at 5 µg/mL for 10
692 min at 37 ˚C, then washed twice with 1x PBS. Cells were placed in Live Cell Imaging Solution (Invitrogen)
693 prior to imaging using Nikon A1R HD25 point scanning confocal with GaAsP and PMT detectors, equipped
694 with an Apo TIRF 60x/1.49 NA objective lens and Ti2 Z-drive. Temperature, humidity, and CO_2
695 concentrations were controlled with a Live Cell environmental chamber (Oko-Lab). Image acquisition were
696 done using NIS-Elements (Nikon Instruments Inc.) and subsequent analysis were performed using Fiji[67].
697
698 *Protein Expression and Purification*
699 A plasmid encoding mTagBFP2-Strep was transformed into *E. coli* BL21 (DE3) pLysS, grown at 37 °C in LB
700 media to OD_{600} 0.5-0.7, induced with 0.5 mM IPTG (Gold Biotechnology), and harvested after 3 h of
701 expression. Cells were resuspended in 25 mL per liter of culture of Buffer A (25 mM HEPES-NaOH pH 7.5,
702 500 mM NaCl, 20 mM imidazole, 0.5 mM dithiothreitol (DTT)) supplemented with 10 µM leupeptin (Sigma
703 Aldrich), 1 µM pepstatin A (Sigma Aldrich), 1 mM phenylmethylsulfonyl fluoride (Sigma Aldrich), 1 mg/mL
704 chicken egg lysozyme (Fisher), and 250 U benzonase nuclease (Sigma Aldrich); and incubated with stirring

705 for 1 h at 4 °C. Cells were then sonicated for 3 min in an ice/water bath with 5 s on / 10 s off pulses. The
706 lysate was then clarified by centrifugation in a JA-25.5 rotor (Beckman Coulter) for 45 min, 15,000 rpm,
707 4 °C. The supernatant was then loaded onto two 5-mL HisTrap columns (Cytiva) plumbed in series
708 equilibrated in Buffer A using a peristaltic pump at 1.5 mL / min flow rate. The column was washed with
709 100 mL of Buffer A and eluted with 20 mL of Buffer B (25 mM HEPES-NaOH pH 7.5, 500 mM NaCl, 300 mM
710 Imidazole, 0.5 mM DTT). The protein was found to be ~95% pure by SDS-PAGE, and the concentration of
711 the eluted material was measured using absorbance signal at 280 nm. The samples were divided into small
712 aliquots, flash frozen in liquid nitrogen and stored at -80 °C.
713
714 *Chol-IP Assays*
715 Prior to running chol-IP assays, input EVs were quantified by SDS-PAGE and immunoblotting to ensure
716 equal inputs of Prom1-Strep and/or Ttyh1-Strep in each assay. EVs were mixed 4:1 with buffer CIA (25
717 mM HEPES-NaOH pH 7.8, 150 mM NaCl, 5 mM $CaCl_2$, 5% n-dodecyl-beta-maltoside (DDM) (Anatrace)) and
718 incubated for 1 h at 4C with end-over-end rotation, protected from ambient light. During incubation,
719 0.025 µL of StrepTactinXT 4Flow resin (IBA) per condition was equilibrated with buffer CIB (25 mM HEPES-
720 NaOH pH 7.8, 150 mM NaCl, 5 mM $CaCl_2$, 1% DDM) in a single pooled reaction. mTagBFP2-Strep was added
721 to the resin at a ratio of 2 µL of 10 nM mTagBFP2-Strep per 1 µL of resin, and incubated for 15 min at 4 °C
722 with end-over-end rotation, protected from ambient light. After one additional wash with buffer CIB, the
723 resin was then divided equally across low-binding 1.5 mL tubes (USA Scientific) so that each condition
724 being tested plus one negative control condition had equal inputs of BFP-labeled resin. The DDM-treated
725 EVs were then added to the appropriate resin tube and incubated for 1 h at 4 °C with end-over-end
726 rotation, protected from ambient light. Each condition was then washed twice with buffer CIB for 5 min
727 at 4C with end-over-end rotation, resuspended in 45 µL of buffer CIB, and stored on ice, protected from
728 light. Each condition was sequentially pipetted with a cut pipette tip onto a glass microscope slide (Fisher)
729 and gently covered with an 18 mm x 18 mm no. 1 glass cover slip (Matsunami) layered on carefully to
730 minimize trapped air bubbles. Montaged images of the resin beads were collected using an Axio Observer
731 TIRF microscope in epifluorescence mode (Zeiss) with a Prime 95B camera (Photometrics) running
732 SlideBook v. 6.0.24 software (3i). Custom scripts were then used to identify resin beads in each image
733 using DAPI (BFP) signal to both identify beads and normalize fluorescence signal in the FITC (BODIPY-
734 cholesterol) or CY5 (AlexaFluor647-cholesterol) channels. Images of all resin particles were manually
735 reviewed to ensure the exclusion of air bubbles, or other non-resin fluorescent artifacts from downstream
736 analysis. Analysis scripts have been made publicly available at https://github.com/tribell4310/bead-assay.

737

738 *Immunopurification Assays*

739 Co-immunopurification assays from EVs containing fluorescently labeled Prom1 or Pcdh21 were
740 performed as described above for the chol-IP assay, using montaged fluorescence imaging for sensitive
741 and quantitative measurements. Prom1-mScarlet was imaged using CY3 and Pcdh21-mNeonGreen using
742 FITC filter sets.

743

744 *BS3 Crosslinking Assay*

745 Bis(sulfosuccinimidyl)suberate (BS3) powder (Thermo Fisher) was dissolved in buffer immediately before
746 use in assays. Briefly, 2 mg of BS3 powder was dissolved to a concentration of 25 mM in 25 mM
747 HEPES-NaOH pH 7.8, 150 mM NaCl, 0.5 mM $CaCl_2$. Two-fold serial dilutions were then prepared in the
748 same buffer down to a lowest stock concentration of 0.8 mM. The assay was started by combining 10 µL
749 of purified EVs with 2.5 µL of each dilution of BS3. As a negative control condition, 10 µL of purified EVs
750 were combined with 2.5 µL of buffer. Reactions were incubated at ambient temperature for 30 min, then
751 Tris-HCl pH 7.4 was added to each reaction at a final concentration of 50 mM and incubated for 15 min to
752 quench unreacted BS3. Samples were analyzed by SDS-PAGE and immunoblotting.

753

754 *Equilibrium Sucrose Gradient Sedimentation Analysis*

755 Linear sucrose gradients were prepared in Seton 7030 tubes using 5% and 30% (w/v) sucrose dissolved
756 in PBS buffer using a Gradient Station IP (BioComp). Freshly prepared gradients were loaded into an
757 SW-41 Ti swinging bucket rotor and 200 µL of the purified EVs were layered atop gradients immediately
758 prior to centrifugation. Samples were centrifuged for 5 h, 22,000 rpm, 4 °C, then fractionated into 13
759 fractions of 930 µL using the Gradient Station IP. Gradient fractions were analyzed by SDS-PAGE and
760 immunoblotting, then quantified as described above.

761

762 *Cholesterol depletion with methyl-beta cyclodextrin*

763 Methyl beta-cyclodextrin (mBCD) (Sigma Aldrich) was dissolved in sterile-filtered PBS buffer to a final
764 concentration of 20 mM, and a two-fold serial dilution series was prepared. For each condition (0 mM,
765 2.5 mM, 5 mM, and 10 mM mBCD), purified EVs were mixed 1:1 with the appropriate mBCD dilution and
766 incubated for 2 h at 37 °C. After the reaction was complete, the EVs were immediately re-purified over a
767 qEV2-35 nm column (Izon) as described above. Prom1 and Ttyh1 content was assessed with equal volumes
768 of re-purified EVs by SDS-PAGE and immunoblotting. Cholesterol in the purified samples was quantified

769 using Amplex Red reagent (Thermo Fisher) according to the manufacturer's protocol, with fluorescence
770 measurements taken using a SpectraMax M5 plate reader (Molecular Devices). EV morphology was
771 characterized by preparing NS-TEM grids with mBCD-treated samples and analyzing the resulting images,
772 as described above.
773
774 **Conflicts of Interest**
775 The authors declare that they have no conflicts of interest with the contents of this article.
776
777 **Data Availability**
778 Electron microscopy datasets and all biochemical data are deposited in a Zenodo repository at
779 doi:10.5281/zenodo.10034616. Custom software packages are available at
780 https://github.com/tribell4310.
781
782 **Supporting Information**
783 This article contains supporting information.
784
785 **Acknowledgments**
786 We thank D. Syau (Harvard Medical School) and members of the Chao lab for helpful feedback, and Z. Li,
787 S. Sterling, R. Walsh, M. Mayer, and S. Rawson from the Harvard Medical School Cryo-EM Center for
788 support with cryo-TEM data collection. We are grateful to Dr. Richard Bouley at the Microscopy Core of
789 the Program in Membrane Biology (PMB) at MGH for providing helpful advice and equipment access for
790 live-cell confocal microscopy. We thank the staff at the Center for Regenerative Medicine (CRM) Flow
791 Cytometry Core Facility for helpful support in cytometry sorting and analysis. This work was supported by
792 National Institutes of Health R35GM142553 (to LHC) and the Helen Hay Whitney Foundation (to TAB). The
793 content is solely the responsibility of the authors and does not necessarily represent the official views of
794 the National Institutes of Health.
795
796 **References**
797 1. Sharkova, M., Chow, E., Erickson, T., and Hocking, J.C. (2023). The morphological and functional
798 diversity of apical microvilli. J. Anat. *242*, 327–353. 10.1111/joa.13781.

799 2. Satir, P., and Christensen, S.T. (2007). Overview of structure and function of mammalian cilia. Annu.
800 Rev. Physiol. *69*, 377–400. 10.1146/annurev.physiol.69.040705.141236.

801 3. Brown, D.A., and London, E. (2000). Structure and Function of Sphingolipid- and Cholesterol-rich
802 Membrane Rafts*. J. Biol. Chem. *275*, 17221–17224. 10.1074/jbc.R000005200.

803 4. Corbeil, D., Marzesco, A.-M., Wilsch-Bräuninger, M., and Huttner, W.B. (2010). The intriguing links
804 between prominin-1 (CD133), cholesterol-based membrane microdomains, remodeling of apical
805 plasma membrane protrusions, extracellular membrane particles, and (neuro)epithelial cell
806 differentiation. FEBS Lett. *584*, 1659–1664. 10.1016/j.febslet.2010.01.050.

807 5. Corbeil, D., Karbanová, J., Fargeas, C.A., and Jászai, J. (2013). Prominin-1 (CD133): Molecular and
808 Cellular Features Across Species. In Prominin-1 (CD133): New Insights on Stem & Cancer Stem Cell
809 Biology Advances in Experimental Medicine and Biology., D. Corbeil, ed. (Springer), pp. 3–24.
810 10.1007/978-1-4614-5894-4_1.

811 6. Yin, A.H., Miraglia, S., Zanjani, E.D., Almeida-Porada, G., Ogawa, M., Leary, A.G., Olweus, J., Kearney,
812 J., and Buck, D.W. (1997). AC133, a Novel Marker for Human Hematopoietic Stem and Progenitor
813 Cells. Blood *90*, 5002–5012. 10.1182/blood.V90.12.5002.

814 7. Miraglia, S., Godfrey, W., Yin, A.H., Atkins, K., Warnke, R., Holden, J.T., Bray, R.A., Waller, E.K., and
815 Buck, D.W. (1997). A Novel Five-Transmembrane Hematopoietic Stem Cell Antigen: Isolation,
816 Characterization, and Molecular Cloning. Blood *90*, 5013–5021. 10.1182/blood.V90.12.5013.

817 8. Corbeil, D., Röper, K., Weigmann, A., and Huttner, W.B. (1998). AC133 Hematopoietic Stem Cell
818 Antigen: Human Homologue of Mouse Kidney Prominin or Distinct Member of a Novel Protein
819 Family? Blood *91*, 2625–2626. 10.1182/blood.V91.7.2625.

820 9. Kemper, K., Tol, M.J.P.M., and Medema, J.P. (2010). Mouse Tissues Express Multiple Splice Variants of
821 Prominin-1. PLOS ONE *5*, e12325. 10.1371/journal.pone.0012325.

822 10. Mak, A.B., Nixon, A.M.L., Kittanakom, S., Stewart, J.M., Chen, G.I., Curak, J., Gingras, A.-C.,
823 Mazitschek, R., Neel, B.G., Stagljar, I., et al. (2012). Regulation of CD133 by HDAC6 Promotes β-
824 Catenin Signaling to Suppress Cancer Cell Differentiation. Cell Rep. *2*, 951–963.
825 10.1016/j.celrep.2012.09.016.

826 11. Yang, Z., Chen, Y., Lillo, C., Chien, J., Yu, Z., Michaelides, M., Klein, M., Howes, K.A., Li, Y.,
827 Kaminoh, Y., et al. (2008). Mutant prominin 1 found in patients with macular degeneration disrupts
828 photoreceptor disk morphogenesis in mice. J. Clin. Invest. *118*, 2908–2916. 10.1172/JCI35891.

829 12. Burgoyne, T., Meschede, I.P., Burden, J.J., Bailly, M., Seabra, M.C., and Futter, C.E. (2015). Rod
830 disc renewal occurs by evagination of the ciliary plasma membrane that makes cadherin-based
831 contacts with the inner segment. Proc. Natl. Acad. Sci. *112*, 15922–15927.
832 10.1073/pnas.1509285113.

833 13. Bolz, H., Ebermann, I., and Gal, A. (2005). Protocadherin-21 (PCDH21), a candidate gene for
834 human retinal dystrophies. Mol. Vis. *11*, 929–933.

835 14. Cohen, B., Chervinsky, E., Jabaly-Habib, H., Shalev, S.A., Briscoe, D., and Ben-Yosef, T. (2012). A
836 novel splice site mutation of CDHR1 in a consanguineous Israeli Christian Arab family segregating
837 autosomal recessive cone-rod dystrophy. Mol. Vis. *18*, 2915–2921.

838 15. Duncan, J.L., Roorda, A., Navani, M., Vishweswaraiah, S., Syed, R., Soudry, S., Ratnam, K.,
839 Gudiseva, H.V., Lee, P., Gaasterland, T., et al. (2012). Identification of a Novel Mutation in the CDHR1
840 Gene in a Family With Recessive Retinal Degeneration. Arch. Ophthalmol. *130*, 1301–1308.
841 10.1001/archophthalmol.2012.1906.

842 16. Henderson, R.H., Li, Z., Aziz, M.M.A.-E., Mackay, D., Scambler, P., Pierce, K., Wright, G., Zaidan,
843 M., Bhattacharya, S.S., and Webster, A.R. (2008). Biallelic Mutation of Protocadherin-21 (pcdh21)
844 Causes Retinal Degeneration in Humans. Invest. Ophthalmol. Vis. Sci. *49*, 3285–3285.

845 17. Nikopoulos, K., Avila-Fernandez, A., Corton, M., Lopez-Molina, M.I., Perez-Carro, R., Bontadelli,
846 L., Gioia, S.A.D., Zurita, O., Garcia-Sandoval, B., Rivolta, C., et al. (2015). Identification of two novel
847 mutations in CDHR1 in consanguineous Spanish families with autosomal recessive retinal dystrophy.
848 Sci. Rep. *5*, 1–10. 10.1038/srep13902.

849 18. Ostergaard, E., Batbayli, M., Duno, M., Vilhelmsen, K., and Rosenberg, T. (2010). Mutations in
850 PCDH21 cause autosomal recessive cone-rod dystrophy. J. Med. Genet. *47*, 665–669.
851 10.1136/jmg.2009.069120.

852 19. Rattner, A., Smallwood, P.M., Williams, J., Cooke, C., Savchenko, A., Lyubarsky, A., Pugh, E.N.,
853 and Nathans, J. (2001). A Photoreceptor-Specific Cadherin Is Essential for the Structural Integrity of
854 the Outer Segment and for Photoreceptor Survival. Neuron *32*, 775–786. 10.1016/S0896-
855 6273(01)00531-1.

856 20. Zacchigna, S., Oh, H., Wilsch-Bräuninger, M., Missol-Kolka, E., Jászai, J., Jansen, S., Tanimoto, N.,
857 Tonagel, F., Seeliger, M., Huttner, W.B., et al. (2009). Loss of the Cholesterol-Binding Protein
858 Prominin-1/CD133 Causes Disk Dysmorphogenesis and Photoreceptor Degeneration. J. Neurosci. *29*,
859 2297–2308. 10.1523/JNEUROSCI.2034-08.2009.

860 21. Eidinger, O., Leibu, R., Newman, H., Rizel, L., Perlman, I., and Ben-Yosef, T. (2015). An intronic
861 deletion in the PROM1 gene leads to autosomal recessive cone-rod dystrophy. Mol. Vis. *21*, 1295–
862 1306.

863 22. Liang, J., She, X., Chen, J., Zhai, Y., Liu, Y., Zheng, K., Gong, Y., Zhu, H., Luo, X., and Sun, X. (2019).
864 Identification of novel PROM1 mutations responsible for autosomal recessive maculopathy with rod-
865 cone dystrophy. Graefes Arch. Clin. Exp. Ophthalmol. *257*, 619–628. 10.1007/s00417-018-04206-w.

866 23. Maw, M.A., Corbeil, D., Koch, J., Hellwig, A., Wilson-Wheeler, J.C., Bridges, R.J.,
867 Kumaramanickavel, G., John, S., Nancarrow, D., Röper, K., et al. (2000). A frameshift mutation in
868 prominin (mouse)-like 1 causes human retinal degeneration. Hum. Mol. Genet. *9*, 27–34.
869 10.1093/hmg/9.1.27.

870 24. Fargeas, C.A. (2013). Prominin-2 and Other Relatives of CD133. In Prominin-1 (CD133): New
871 Insights on Stem & Cancer Stem Cell Biology Advances in Experimental Medicine and Biology., D.
872 Corbeil, ed. (Springer), pp. 25–40. 10.1007/978-1-4614-5894-4_2.

873 25. Hori, A., Nishide, K., Yasukuni, Y., Haga, K., Kakuta, W., Ishikawa, Y., Hayes, M.J., Ohnuma, S.,
874 Kiyonari, H., Kimura, K., et al. (2019). Prominin-1 Modulates Rho/ROCK-Mediated Membrane
875 Morphology and Calcium-Dependent Intracellular Chloride Flux. Sci. Rep. *9*, 15911. 10.1038/s41598-
876 019-52040-9.

877 26. Röper, K., Corbeil, D., and Huttner, W.B. (2000). Retention of prominin in microvilli reveals
878 distinct cholesterol-based lipid micro-domains in the apical plasma membrane. Nat. Cell Biol. *2*, 582–
879 592. 10.1038/35023524.

880 27. Dubreuil, V., Marzesco, A.-M., Corbeil, D., Huttner, W.B., and Wilsch-Bräuninger, M. (2007).
881 Midbody and primary cilium of neural progenitors release extracellular membrane particles enriched
882 in the stem cell marker prominin-1. J. Cell Biol. *176*, 483–495. 10.1083/jcb.200608137.

883 28. Marzesco, A.-M., Janich, P., Wilsch-Bräuninger, M., Dubreuil, V., Langenfeld, K., Corbeil, D., and
884 Huttner, W.B. (2005). Release of extracellular membrane particles carrying the stem cell marker
885 prominin-1 (CD133) from neural progenitors and other epithelial cells. J. Cell Sci. *118*, 2849–2858.
886 10.1242/jcs.02439.

887 29. Wood, C.R., and Rosenbaum, J.L. (2015). Ciliary ectosomes: transmissions from the cell's
888 antenna. Trends Cell Biol. *25*, 276–285. 10.1016/j.tcb.2014.12.008.

889 30. Hurbain, I., Macé, A.-S., Romao, M., Prince, E., Sengmanivong, L., Ruel, L., Basto, R., Thérond,
890 P.P., Raposo, G., and D'Angelo, G. (2022). Microvilli-derived extracellular vesicles carry Hedgehog
891 morphogenic signals for Drosophila wing imaginal disc development. Curr. Biol. *32*, 361-373.e6.
892 10.1016/j.cub.2021.11.023.

893 31. Campbell, H.D., Kamei, M., Claudianos, C., Woollatt, E., Sutherland, G.R., Suzuki, Y., Hida, M.,
894 Sugano, S., and Young, I.G. (2000). Human and Mouse Homologues of the Drosophila melanogaster
895 tweety (tty) Gene: A Novel Gene Family Encoding Predicted Transmembrane Proteins. Genomics *68*,
896 89–92. 10.1006/geno.2000.6259.

897 32. Matthews, C.A., Shaw, J.E., Hooper, J.A., Young, I.G., Crouch, M.F., and Campbell, H.D. (2007).
898 Expression and evolution of the mammalian brain gene Ttyh1. J. Neurochem. *100*, 693–707.
899 10.1111/j.1471-4159.2006.04237.x.

900 33. Halleran, A.D., Sehdev, M., Rabe, B.A., Huyck, R.W., Williams, C.C., and Saha, M.S. (2015).
901 Characterization of tweety gene (ttyh1-3) expression in Xenopus laevis during embryonic
902 development. Gene Expr. Patterns *17*, 38–44. 10.1016/j.gep.2014.12.002.

903 34. Bae, Y., Kim, A., Cho, C.-H., Kim, D., Jung, H.-G., Kim, S.-S., Yoo, J., Park, J.-Y., and Hwang, E.M.
904 (2019). TTYH1 and TTYH2 Serve as LRRC8A-Independent Volume-Regulated Anion Channels in Cancer
905 Cells. Cells *8*, 562. 10.3390/cells8060562.

906 35. Han, Y.-E., Kwon, J., Won, J., An, H., Jang, M.W., Woo, J., Lee, J.S., Park, M.G., Yoon, B.-E., Lee,
907 S.E., et al. (2019). Tweety-homolog (Ttyh) Family Encodes the Pore-forming Subunits of the Swelling-
908 dependent Volume-regulated Anion Channel (VRACswell) in the Brain. Exp. Neurobiol. *28*, 183–215.
909 10.5607/en.2019.28.2.183.

910 36. Li, B., Hoel, C.M., and Brohawn, S.G. (2021). Structures of Tweety Homolog Proteins TTYH2 and
911 TTYH3 reveal a Ca2+-dependent switch from intra- to inter-membrane dimerization
912 10.1101/2021.08.15.456437.

913 37. Sukalskaia, A., Straub, M.S., Deneka, D., Sawicka, M., and Dutzler, R. (2021). Cryo-EM structures
914 of the TTYH family reveal a novel architecture for lipid interactions. Nat. Commun. *12*, 4893.
915 10.1038/s41467-021-25106-4.

916 38. Melvin, E., Shlush, E., Giladi, M., and Haitin, Y. (2021). TTYH family members form tetrameric
917 complexes within the cell membrane. Preprint at bioRxiv, 10.1101/2021.09.05.459021
918 10.1101/2021.09.05.459021.

919 39. Jung, E., Osswald, M., Blaes, J., Wiestler, B., Sahm, F., Schmenger, T., Solecki, G., Deumelandt, K.,
920 Kurz, F.T., Xie, R., et al. (2017). Tweety-Homolog 1 Drives Brain Colonization of Gliomas. J. Neurosci.
921 *37*, 6837–6850. 10.1523/JNEUROSCI.3532-16.2017.

922 40. Stefaniuk, M., Swiech, L., Dzwonek, J., and Lukasiuk, K. (2010). Expression of Ttyh1, a member of
923 the Tweety family in neurons in vitro and in vivo and its potential role in brain pathology. J.
924 Neurochem. *115*, 1183–1194. 10.1111/j.1471-4159.2010.07023.x.

925 41. Wiernasz, E., Kaliszewska, A., Brutkowski, W., Bednarczyk, J., Gorniak, M., Kaza, B., and Lukasiuk,
926 K. (2014). Ttyh1 Protein is Expressed in Glia In Vitro and Shows Elevated Expression in Activated
927 Astrocytes Following Status Epilepticus. Neurochem. Res. *39*, 2516–2526. 10.1007/s11064-014-1455-
928 3.

929 42. Kemper, K., Sprick, M.R., Bree, M. de, Scopelliti, A., Vermeulen, L., Hoek, M., Zeilstra, J., Pals,
930 S.T., Mehmet, H., Stassi, G., et al. (2010). The AC133 Epitope, but not the CD133 Protein, Is Lost upon
931 Cancer Stem Cell Differentiation. Cancer Res. *70*, 719–729. 10.1158/0008-5472.CAN-09-1820.

932 43. Huttner, W.B., Schiebler, W., Greengard, P., and De Camilli, P. (1983). Synapsin I (protein I), a
933 nerve terminal-specific phosphoprotein. III. Its association with synaptic vesicles studied in a highly
934 purified synaptic vesicle preparation. J. Cell Biol. *96*, 1374–1388. 10.1083/jcb.96.5.1374.

935 44. Fantini, J., and Barrantes, F.J. (2013). How cholesterol interacts with membrane proteins: an
936 exploration of cholesterol-binding sites including CRAC, CARC, and tilted domains. Front. Physiol. *4*.
937 10.3389/fphys.2013.00031.

938 45. Boulanger-Scemama, E., El Shamieh, S., Démontant, V., Condroyer, C., Antonio, A., Michiels, C.,
939 Boyard, F., Saraiva, J.-P., Letexier, M., Souied, E., et al. (2015). Next-generation sequencing applied to
940 a large French cone and cone-rod dystrophy cohort: mutation spectrum and new genotype-
941 phenotype correlation. Orphanet J. Rare Dis. *10*, 85. 10.1186/s13023-015-0300-3.

942 46. Jumper, J., Evans, R., Pritzel, A., Green, T., Figurnov, M., Ronneberger, O., Tunyasuvunakool, K.,
943 Bates, R., Žídek, A., Potapenko, A., et al. (2021). Highly accurate protein structure prediction with
944 AlphaFold. Nature *596*, 583–589. 10.1038/s41586-021-03819-2.

945 47. Zidovetzki, R., and Levitan, I. (2007). Use of cyclodextrins to manipulate plasma membrane
946 cholesterol content: Evidence, misconceptions and control strategies. Biochim. Biophys. Acta BBA -
947 Biomembr. *1768*, 1311–1324. 10.1016/j.bbamem.2007.03.026.

948 48. Salinas, R.Y., Pearring, J.N., Ding, J.-D., Spencer, W.J., Hao, Y., and Arshavsky, V.Y. (2017).
949 Photoreceptor discs form through peripherin-dependent suppression of ciliary ectosome release. J.
950 Cell Biol. *216*, 1489–1499. 10.1083/jcb.201608081.

951 49. Lorent, J.H., Levental, K.R., Ganesan, L., Rivera-Longsworth, G., Sezgin, E., Doktorova, M., Lyman,
952 E., and Levental, I. (2020). Plasma membranes are asymmetric in lipid unsaturation, packing and
953 protein shape. Nat. Chem. Biol. *16*, 644–652. 10.1038/s41589-020-0529-6.

954 50. Kanazawa, T., Takematsu, H., Yamamoto, A., Yamamoto, H., and Kozutsumi, Y. (2008). Wheat
955 germ agglutinin stains dispersed post-golgi vesicles after treatment with the cytokinesis inhibitor
956 psychosine. J. Cell. Physiol. *215*, 517–525. 10.1002/jcp.21328.

957 51. Mak, A.B., Blakely, K.M., Williams, R.A., Penttilä, P.-A., Shukalyuk, A.I., Osman, K.T., Kasimer, D.,
958 Ketela, T., and Moffat, J. (2011). CD133 Protein N-Glycosylation Processing Contributes to Cell Surface
959 Recognition of the Primitive Cell Marker AC133 Epitope *. J. Biol. Chem. *286*, 41046–41056.
960 10.1074/jbc.M111.261545.

961 52. Imperiali, B., and O'Connor, S.E. (1999). Effect of N-linked glycosylation on glycopeptide and
962 glycoprotein structure. Curr. Opin. Chem. Biol. *3*, 643–649. 10.1016/S1367-5931(99)00021-6.

963 53. Fargeas, C.A., Huttner, W.B., and Corbeil, D. (2007). Nomenclature of prominin-1 (CD133) splice
964 variants – an update. Tissue Antigens *69*, 602–606. 10.1111/j.1399-0039.2007.00825.x.

965 54. Elegheert, J., Behiels, E., Bishop, B., Scott, S., Woolley, R.E., Griffiths, S.C., Byrne, E.F.X., Chang,
966 V.T., Stuart, D.I., Jones, E.Y., et al. (2018). Lentiviral transduction of mammalian cells for fast, scalable
967 and high-level production of soluble and membrane proteins. Nat. Protoc. *13*, 2991–3017.
968 10.1038/s41596-018-0075-9.

969 55. Kutner, R.H., Zhang, X.-Y., and Reiser, J. (2009). Production, concentration and titration of
970 pseudotyped HIV-1-based lentiviral vectors. Nat. Protoc. *4*, 495–505. 10.1038/nprot.2009.22.

971 56. Schneider, C.A., Rasband, W.S., and Eliceiri, K.W. (2012). NIH Image to ImageJ: 25 years of image
972 analysis. Nat. Methods *9*, 671–675. 10.1038/nmeth.2089.

973 57. Sayers, E.W., Bolton, E.E., Brister, J.R., Canese, K., Chan, J., Comeau, D.C., Connor, R., Funk, K.,
974 Kelly, C., Kim, S., et al. (2022). Database resources of the national center for biotechnology
975 information. Nucleic Acids Res. *50*, D20–D26. 10.1093/nar/gkab1112.

976 58. Paysan-Lafosse, T., Blum, M., Chuguransky, S., Grego, T., Pinto, B.L., Salazar, G.A., Bileschi, M.L.,
977 Bork, P., Bridge, A., Colwell, L., et al. (2023). InterPro in 2022. Nucleic Acids Res. *51*, D418–D427.
978 10.1093/nar/gkac993.

979 59. Sonnhammer, E.L., von Heijne, G., and Krogh, A. (1998). A hidden Markov model for predicting
980 transmembrane helices in protein sequences. Proc. Int. Conf. Intell. Syst. Mol. Biol. *6*, 175–182.

981 60. Katoh, K., Misawa, K., Kuma, K., and Miyata, T. (2002). MAFFT: a novel method for rapid multiple
982 sequence alignment based on fast Fourier transform. Nucleic Acids Res. *30*, 3059–3066.
983 10.1093/nar/gkf436.

984 61. Minh, B.Q., Schmidt, H.A., Chernomor, O., Schrempf, D., Woodhams, M.D., von Haeseler, A., and
985 Lanfear, R. (2020). IQ-TREE 2: New Models and Efficient Methods for Phylogenetic Inference in the
986 Genomic Era. Mol. Biol. Evol. *37*, 1530–1534. 10.1093/molbev/msaa015.

987 62. Kalyaanamoorthy, S., Minh, B.Q., Wong, T.K.F., von Haeseler, A., and Jermiin, L.S. (2017).
988 ModelFinder: fast model selection for accurate phylogenetic estimates. Nat. Methods *14*, 587–589.
989 10.1038/nmeth.4285.

990 63. Anisimova, M., and Gascuel, O. (2006). Approximate Likelihood-Ratio Test for Branches: A Fast,
991 Accurate, and Powerful Alternative. Syst. Biol. *55*, 539–552. 10.1080/10635150600755453.

992 64. Clamp, M., Cuff, J., Searle, S.M., and Barton, G.J. (2004). The Jalview Java alignment editor.
993 Bioinformatics *20*, 426–427. 10.1093/bioinformatics/btg430.

994 65. Vaughan, T.G. (2017). IcyTree: rapid browser-based visualization for phylogenetic trees and
995 networks. Bioinformatics *33*, 2392–2394. 10.1093/bioinformatics/btx155.

996 66. Livingstone, C.D., and Barton, G.J. (1993). Protein sequence alignments: a strategy for the
997 hierarchical analysis of residue conservation. Bioinformatics *9*, 745–756.
998 10.1093/bioinformatics/9.6.745.

999 67. Schindelin, J., Arganda-Carreras, I., Frise, E., Kaynig, V., Longair, M., Pietzsch, T., Preibisch, S.,
1000 Rueden, C., Saalfeld, S., Schmid, B., et al. (2012). Fiji: an open-source platform for biological-image
1001 analysis. Nat. Methods *9*, 676–682. 10.1038/nmeth.2019.

1002

1003 ***Supporting Information***

1004

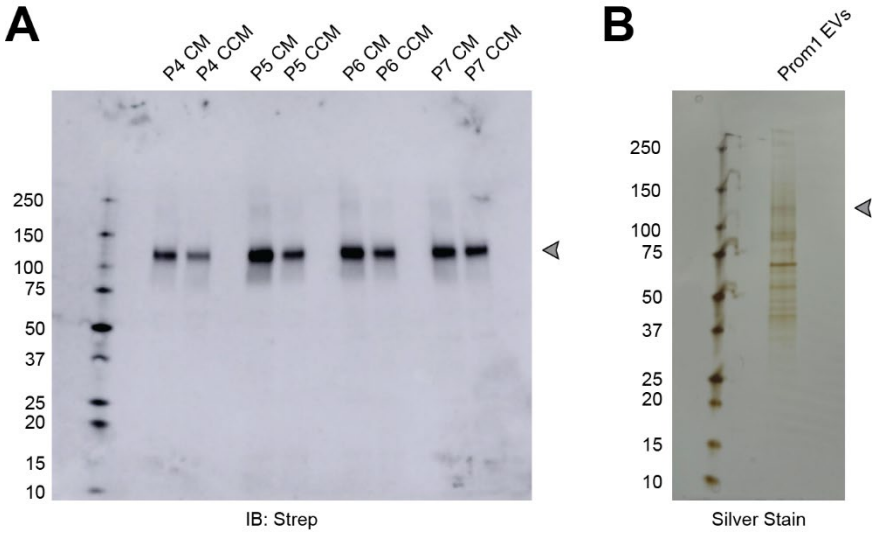

1005

1006 **Figure S1. (A)** Anti-Strep immunoblot of conditioned media (CM) or clarified conditioned media (CCM)
1007 from a stable polyclonal Expi293 cell line expressing lentiviral-transduced Prom1-Strep. Arrowhead
1008 indicates the expected position of glycosylated Prom1-Strep. P4, P5, P6, and P7 indicate the passage
1009 number of the suspension cell culture. **(B)** Total protein stain of purified Prom1-Strep EVs. Arrowhead
1010 indicates the expected position of glycosylated Prom1-Strep.

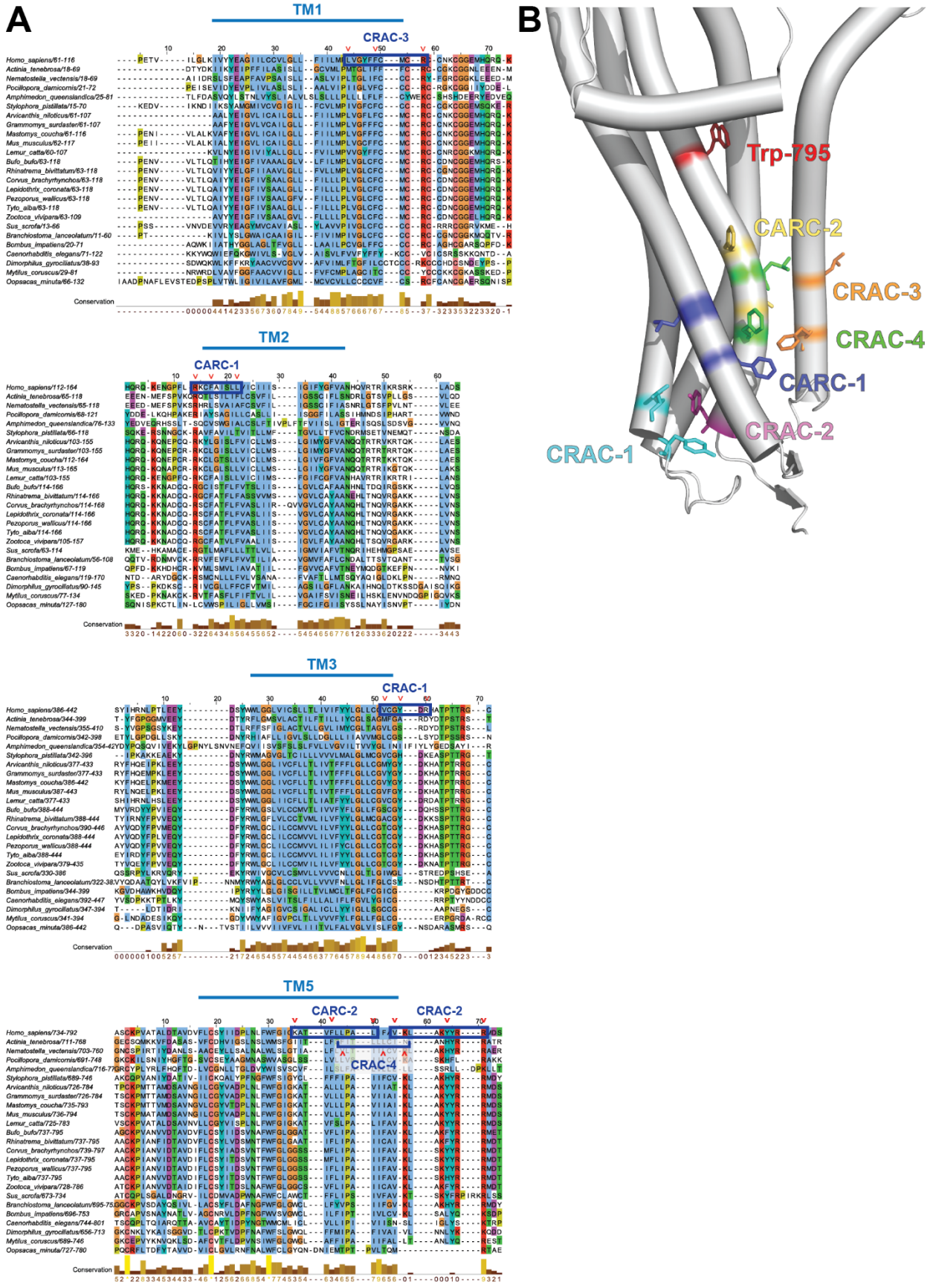
A
TM1
CRAC-3
TM2
CARC-1
TM3
CRAC-1
TM5
CARC-2
CRAC-2
CRAC-4
Conservation
B
Trp-795
CARC-2
CRAC-3
CRAC-4
CARC-1
CRAC-2
CRAC-1

1011

1012

1013 **Figure S2. (A)** Multiple sequence alignment of metazoan Prom1 focused on transmembrane domains 1,
1014 2, 3, and 5, with human CRAC and CARC domains highlighted. Red carats indicate key charged, aromatic,
1015 or hydrophobic residues that define the CRAC and CARC domains. Alignment visualized using Jalview[64].
1016 **(B)** Trp-795, CRAC-1, CRAC-2, CRAC-3, CRAC-4, CARC-1, and CARC-2 mutation sites superposed onto an
1017 AlphaFold2 model[46] of the transmembrane domain of Prom1.

1018

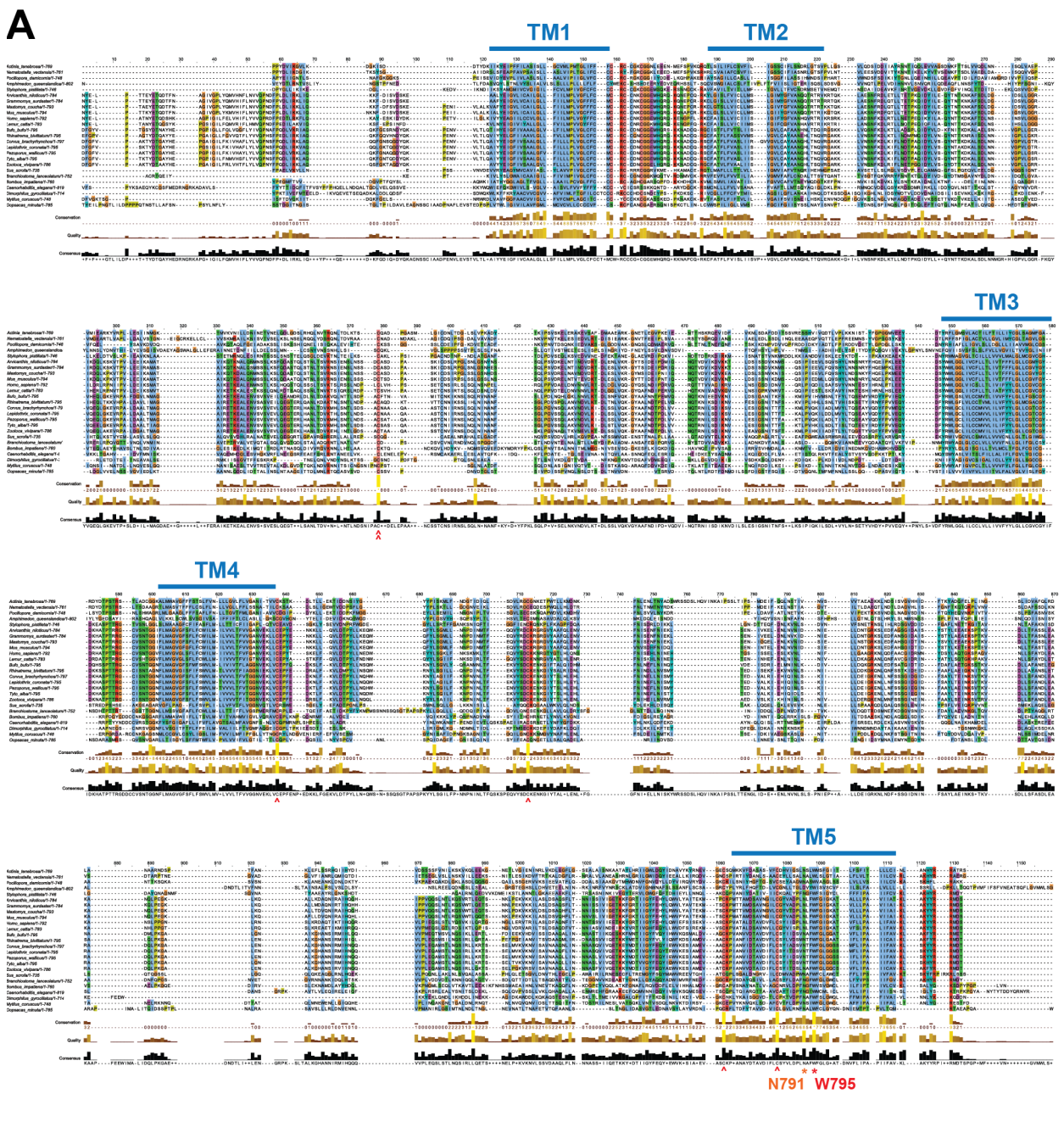

1019

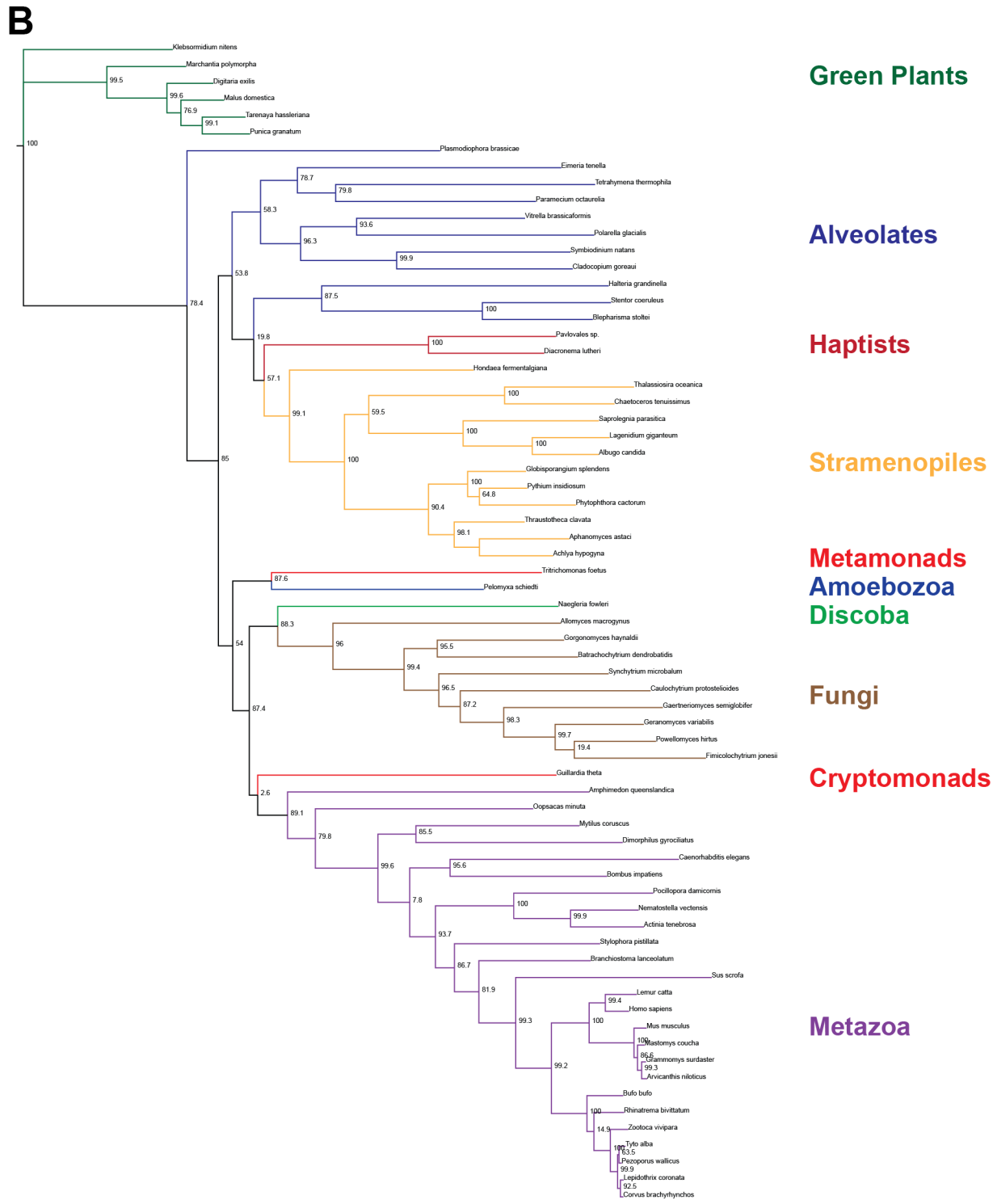

Figure S3. (A) Multiple-sequence alignment of prominin sequences from metazoa with the five transmembrane segments indicated. Red asterisk indicates perfectly conserved non-cysteine residues. Orange asterisk indicates less-than-perfectly conserved non-cysteine residues of interest. Red carat indicates cysteines predicted to form internal disulfides. Double red carat indicates cysteines that are not predicted to form internal disulfides. Alignment visualized using Jalview[64]. **(B)** Inferred phylogenetic

1026 relationships between putative prominin homologs identified across eukaryotes. Node labels indicate
1027 ALRT branch supports[63]. Tree visualized using IcyTree[65].

1028

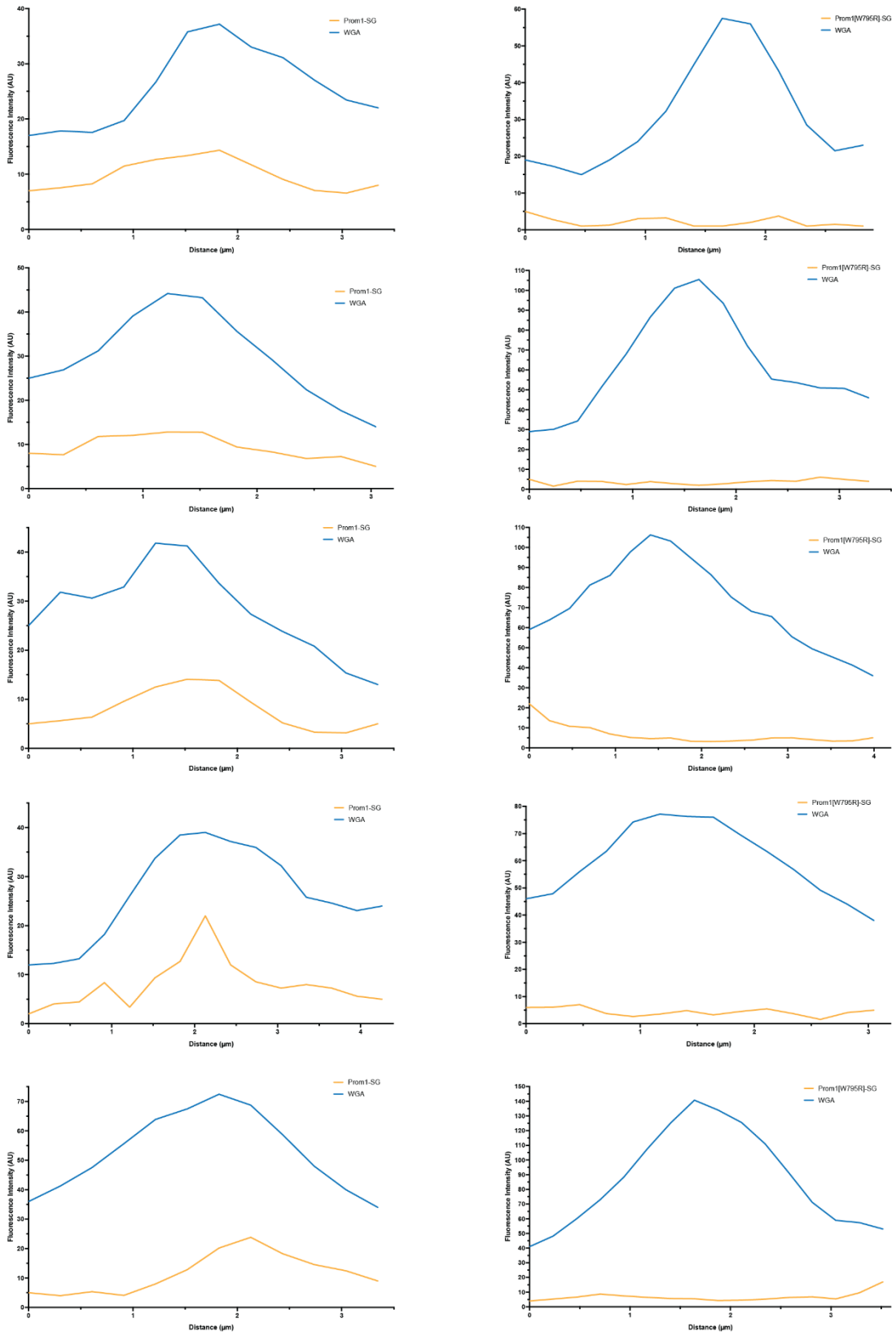
Prom1-SG
WGA
Prom1[W795R]-SG
WGA
Fluorescence Intensity (AU)
Distance (µm)

1029

1030

1031 **Figure S4.** Line scan traces across cell junctions (n = 5) for plasma membrane (WGA) (blue) or Prom1-
1032 mStayGold fluorescence signal for WT (left panels) or W795R (right panels) Prom1 (yellow).

1033

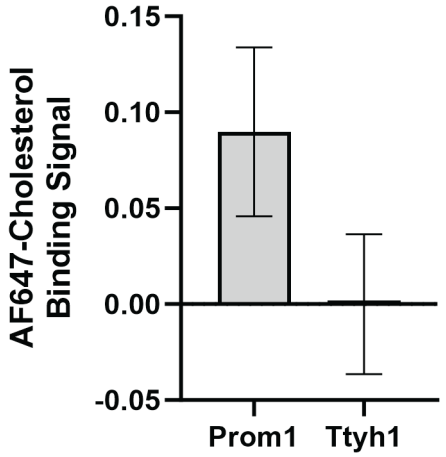

1034

1035 **Figure S5.** Cholesterol co-immunopurification (Chol-IP) measurement of AlexaFluor647-cholesterol
1036 binding in Prom1-Strep or Ttyh1-Strep EVs. Error bars indicate S.D. (n = 3).

1037

1038

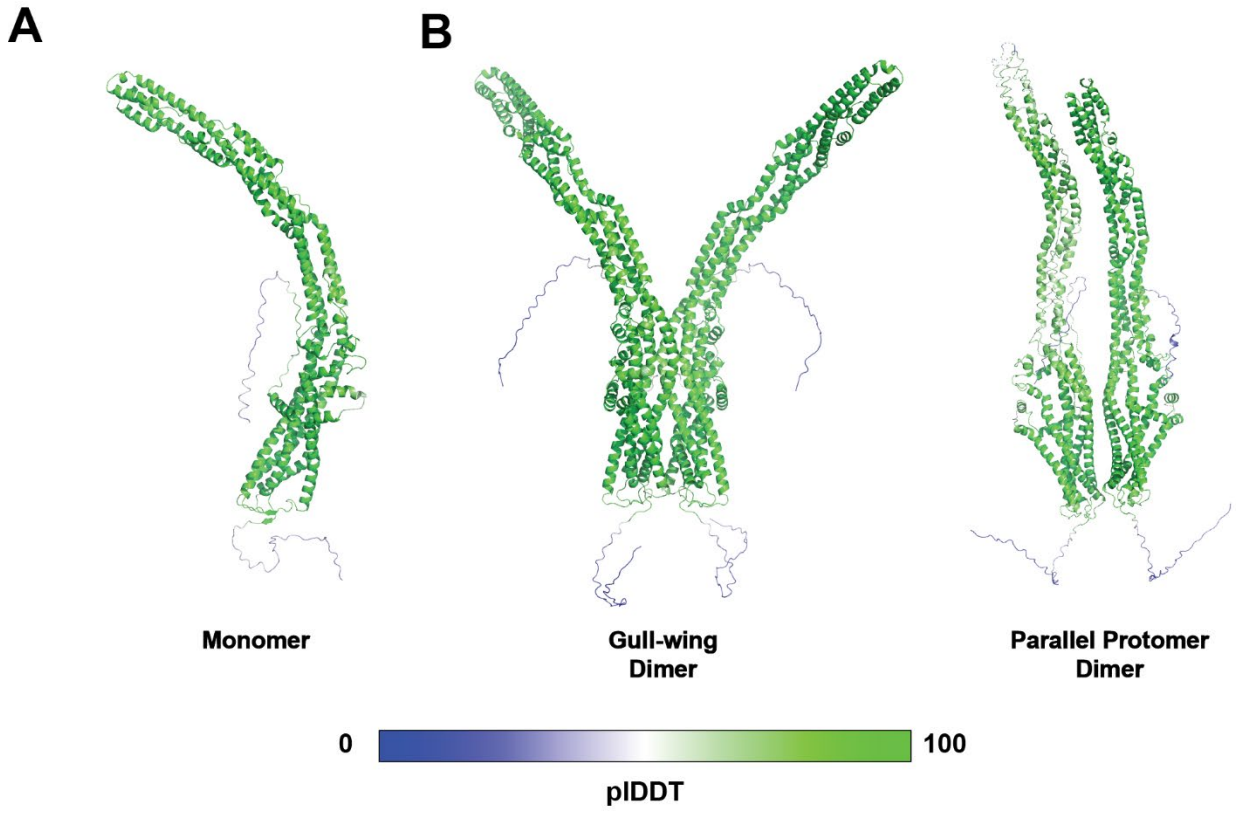

1039

1040

1041 **Figure S6.** AlphaFold2[46] plDDT confidence scores mapped onto **(A)** Prom1 monomer model and **(B)**
1042 Prom1 dimer models.

1043

Prom1 Mutant	Specific Mutations
Wild-type (WT)	- -
CRAC-1	V460A, Y463L
CRAC-2	Y819L
CRAC-3	L125A, F130L
CRAC-4	L806A, F811L
CARC-1	F158L, L162A, L163A
CARC-2	F804L, L806A, L809A
F62L	F62L
L161T	L161T
G454V	G454V
F505L	F505L
N791D	N791D
F794L	F794L
W795L	W795L
W795R	W795R
F796L	F796L

1044

1045 **Table ST1.** Prom1 mutants used in this study. All mutants are adapted from isoform S1 (NCBI accession
1046 NP_001139319.1).

1047

1048 **Movie SM1.** Live-cell confocal fluorescence microscopy of stable mStayGold-tagged WT Prom1 (Prom1-
1049 SG) (yellow) HeLa cells stained with wheat germ agglutinin (WGA) conjugated with Alexa Fluor 647 to
1050 label plasma membrane and intracellular vesicles (blue). Video consists of z-stack images acquired at 0.2
1051 µm step size, assembled from basal to apical side.

1052

1053 **Movie SM2.** Live-cell confocal fluorescence microscopy of stable mStayGold-tagged W795R Prom1
1054 (Prom1[W795R]-SG) (yellow) HeLa cells stained with wheat germ agglutinin (WGA) conjugated with
1055 Alexa Fluor 647 to label plasma membrane and intracellular vesicles (blue). Video consists of z-stack
1056 images acquired at 0.2 µm step size, assembled from basal to apical side.